NTNU
Norwegian University of
Science and Technology

Experimental and Numerical Investigation of Floating Solar Islands

Petter Plünneke Borvik

Marine Technology
Submission date: June 2017
Supervisor: Trygve Kristiansen, IMT

Norwegian University of Science and Technology
Department of Marine Technology

Preface

This report presents the result of a master thesis in marine hydrodynamics for Marine Technology, at the Norwegian University of Science and Technology. Two models of a solar island are made and tested in current, and both regular and irregular waves. In the experiment acceleration in vertical direction, forces in the mooring lines and wave elevation were measured. The results obtained from the experiment will be presented and compared with a numerical model.

The work done during the master is mainly experimental. The theory is used to support the results obtained from the experiment.

A special thanks to my supervisor Professor Trygve Kristiansen, for informative discussion about the experimental results, helping with the theory and with the experimental set-up. Thanks to Odd Magnus Faltisen for guidance during the work. Ole Erik Vinje for helping and assisting in making of the models. Terje Røsten and Torgeir Whal for helping with the experimental work. Peng Li for the comparison between the theory.

Trondheim 10.06.2017

Petter Borvik

Summary

In this master thesis, the dynamical behavior of a floating solar island in waves and current has been investigated. The solar island consists of a torus were the inner part is covered with a membrane. Underneath the membrane an overpressure is applied to support the weight of the photovoltaics panels. A skirt is hanging from the side to prevent leakage of the pressure. This thesis will not go into detail where all the possible placements of the island are, but one alternative is at the coast outside West Africa.

The investigation has been done through model testing. Two different configurations of the solar island were investigated; a model made with an elastic torus and a model with a rigid torus. The other parts of the model were equal. The models are compared in regular waves with height-to-wave length ratio 1/30 and wave period between 0.6-1.6 s, regular waves and current and irregular waves.

A numerical model for the heave response has been developed based on the theory for a floating torus and a surface effect ship, by use of linear potential flow theory. The experimental results are in good agreement with the numerical result. The membrane will lead to larger vertical motion for small wave frequencies and a reduction of the response for high wave frequencies. Another effect of the membrane is that the vertical acceleration and force in the mooring lines gets increased. The largest difference between the two models are the global behavior, since the elastic model is able to follow the waves.

Out of water and over-topping of waves were observed. These non-linear phenomena can lead to flooding of the island. Flooding for both models were observed in; regular waves with steepness 1/20 and period $T = 12.1\,\mathrm{s}$ and irregular waves with peak period $T_p \geq 12.0\,\mathrm{s}$ and significant wave height, $H_s > 5\,\mathrm{m}$.

Further investigation of the solar island is needed to include the effect of the membrane and skirt in the numerical model of the response in horizontal and vertical direction.

Sammendrag

Denne masteroppgaven, utført ved "Marine Technology, at the Norwegian University of Science and Technology", har undersøkt den dynamiske oppførselen til en flytende soløy utsatt for strøm og bølger. Soløyen består av et ringformet flyteelemt, torus, og en membran som dekker den indre ringen. Under membranen er det et overtrykk som skal hjelpe til med å bære vekten av solcellepanelene. For å hindre lekkasje henger det ned et skjørt fra siden av torusen. Denne oppgaven går ikke i detalj for mulig plasseringer av soløyen, men et alternativ kan være utenfor kysten av Vest-Afrika.

Undersøkelsen har blitt gjort gjennom modelltesting. To ulike versjoner av soløyen har blitt undersøkt. En modell er laget med en elastisk torus og en modell med en stiv torus. De andre delene av soløyene er identiske. Modellene er sammenlignet i regulære bølger med høyde til lengde ratio 1/30 og bølgeperiode mellom T =0.6-1.6 s, regulære bølger med strøm og irregulære bølger.

En numerisk modell for torusens hiv-bevegelse har blitt laget basert på teori for hiv-bevegelsen til en flytende torus og teorien for "Surface effect ships", ved hjelp av lineær potensialteori. De eksperimentelle resultatene er i god overenstemmelse med den numeriske modellen. Membranen vil føre til høyere vertikal bevegelse for små bølgefrekvenser og en reduksjon for høye bølgefrekvenser. En annen effekt av membranen er at den vertikale akselerasjonen og kraften i fortøyningslinene øker. Den største forskjellen mellom modellene er den samlede oppførselen, fordi den elastiske modellen kan følge bølgene.

"Ut-av-vann" og "overtopping" av soløyen på grunn av bølgene ble observert. Disse ulineære fenomenene kan føre til overforsvømmelse av soløyen. Overforsvømmelse ble observert for begge modellen for; regulære bølger med steilhet 1/20 og periode T = 12.1 s, irregulære bølger med topp-periode $T_p \geq 12.0\,\mathrm{s}$ og signifikant bølgehøyde $H_s > 5\,\mathrm{m}$.

Videre undersøkelse av soløyen er nødvendig for å inkludere effekten av membranen og skjørtet i den numeriske modellen for responsen i horisontal og vertikal retning.

Table of Contents

List of Tables

Chapter 1

Introduction

Today modern mobility, aeronautics, shipping and long-haul automotive requires high energy density liquid fuel, which is coming from fossil fuels. At this date, there is no practical alternative to liquid carbon-based energy carries. An idea proposed by Frode Mo, department of Physics NTNU, is to use solar energy to the extraction of hydrogen and CO_2 from seawater to create liquid methanol fuel [Mo, Personal communication (2016)].

Due to limited available space on earth a floating solar island able to operate in open seas is proposed. Today there are approximately twenty different types of solar island that exists. These have all been in enclosed water bodies, such as reservoirs, ponds and small lakes (Trapani & Redón Santafé, 2015). Floating photovolatics (PV) system is found to have 11 % better efficiency than overland system (Choi, 2014). Developers are looking to expand the idea into open seas. Concepts proposed are flexible thin structures able to undulate with the waves, or conventional rigid PV arrays that can be submerged in rough water conditions.

The design proposed for the floating solar island is an outer torus, e.q steel ring or high-density polyethylene (HDPE) floaters used in fish farms. Where the inner part is covered with a membrane that is carrying the PV panels. To support the weight of the panels, an overpressure is applied below the membrane. Only about 5 mbar overpressure is needed to carry a load of 50 kg/m. The novel design is chosen due to low complexity and enables a simple turning of the platform (CSEM, 2007). A skirt hanging from the side with weighted ballast is proposed to prevent leakage of the pressure. Figure 1.1 shows an artist impression of the floating solar island.

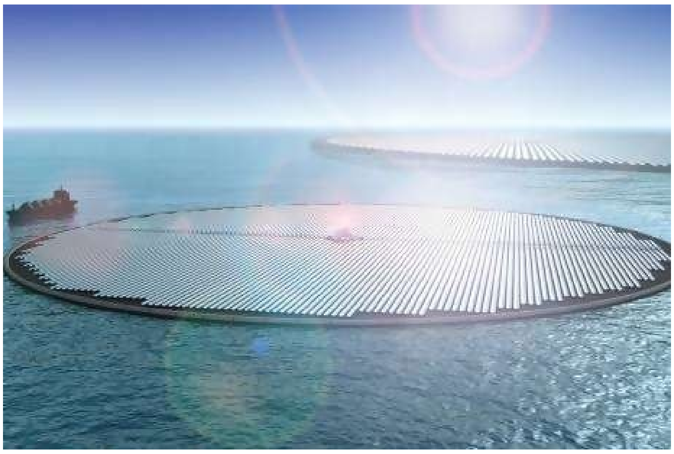

Figure 1.1: Artistic impression of the floating solar island in open sea (computer graphic). The photo is taken from (CSEM, 2007).

A land based prototype of the solar island is built in the emirate Ras Al-Khaimah (RAK) (CSEM, 2007). The prototype is made out of steel with a diameter of 86 m, cross-sectional diameter of 2 m and 6 mm thickness.

1.1 Literature Review

1.1.1 Air Cushions

The use of air cushions to support very large floating structures has been known for a long time in the offshore industry. The applications have mainly been related to a temporary increase in the buoyancy of large-bottom-founded structures for the purpose of transit a shallow building dock to deeper water (Pinkster & Scholte, 2001). Air cushions is also used in Surface Effects Ships (SES) in order reduce the resistance in water (Odd M Faltinsen, 2005).

Pinkster and Fauzi (1997) developed a computational method to determine the effects of air cushions on a large floating structure in waves. A simple circularly shaped pontoon covered with an air cushion is study by use of a linear three-dimensional potential theory with a linearized adiabatic law for the air pressure in the cushion. The air cushion is passive and there is no air leakage or induction. The results show that one of the main effects of the air cushion is very substantially reduction of the static stability of the structure. Another effect of the air cushion is that the heave motion at higher wave frequencies is considerably reduced. The heave response is however increased for lower wave frequencies.

Lee and Newman (2000) study the possible importance of acoustic resonance for the heave and pitch motion. The computational results indicated that the most important resonant response does not occur at these frequencies. The resonant response is explained by the balance between the body inertia force and the appropriate stiffness coefficient for each mode. In heave, the stiffness includes both hydrostatic and aerostatic components, which are in comparable orders of magnitude, whereas for pitch the hydrostatic restoring coefficient is dominant. Thus, the heave resonant frequency is substantially larger than for pitch.

1.1.2 Floating Torus

J. N. Newman (1977b) investigated the motions of a rigid floating slender torus in incident waves. The investigation was done by using slender-body theory. In addition, the forces were investigated, the peaks in the hydrodynamic forces was explained by standing waves within the tours.

When analyzing the wave loads on circular floaters made by HDPE hydroelasticity matters. Odd M. Faltinsen (2011) consider the hydroelasticity of the torus and derived a slender-body theory based on a rigid free-surface condition of the wave effects on the torus by neglecting current.

Dong, Hao, Zhao, Zong, and Gui (2010) proposed an analytically method to analyze the elastic deformation of a circular ring subjected to water waves. The analytic solution is based on Euler's laws and curved beam theory do describe the six-degree-of-freedom motion and elastic deformation. The wave force was evaluated by use of Morrison formula. Experimental data are in agreement with the analytic results.

Odd M. Faltinsen (2012) expand the solution in (Odd M. Faltinsen, 2011) to be valid for a classical linear free-surface condition. Li and Faltinsen (2012) used the results form (Odd M. Faltinsen, 2012) and a Haskind-type expression for the wave excitation loads, to describe the wave-induced vertical response. They predicted that the vertical motion of the floater followed the beam equation. A higher order version of WAMIT was used to verify the analytic solution. The results showed that 3D frequency-dependent hydrodynamic interaction on the scale of the torus diameter is significant.

Li, Faltinsen, and Greco (2014) studied the wave-induced acceleration of an elastic circular collar numerical and experimental. A model with a torus diameter at 1.5m, and a bending stiffness equal to 0.464 Nm^2 was tested in regular waves. The floater where moored with four nearly horizontal moorings with crow feet. The experimental results where compared with the low-frequency slender-body theory. Experimental results showed good agreement for the first harmonic component of vertical acceleration, at front, aft and side of the floater. The results also showed that the higher-order harmonics of the accelerations matter.

Li, Faltinsen, and Lugni (2016) studied the nonlinear wave-induced vertical accelerations of a floating torus in regular waves. A model with a floater diameter at 1.5 m and a bending stiffness equal to 23.74 Nm^2, that is about 100 times the bending stiffness used in (Li et al., 2014), was tested in regular waves. In the experiment, the floater was attached with four nearly horizontal mooring lines, at front, aft, left and right. For height-to-wave length ratio 1/120 reasonable agreement is obtained with linear and partly second-order potential-flow theory. The experiment documented the importance of 3D flow, hydroelasticity and strong hydrodynamic frequency dependency when studying the torus in waves.

1.2 Scope of Work

The main scope of this master thesis is experimental investigation of the dynamical behavior for the described solar island in waves and current. The study is done to find the physical effects so that the design can be used and developed to be able to operate in open seas.

For the idea to be feasible the design of the structure needs to be inexpensive. Steel is an expensive material and can lead to underside jerks and slamming in waves. Using the technology in aquaculture an alternative is to use the cheaper material HDPE floaters. Use of HDPE floaters requires moderate sea states. Moderate sea states can be found by using existing wave data which can be found in Hogben, Olliver, Dacunha, and British Maritime Technology (1986). Other limitations are water depth, isolation rate and ice coverage during winter. The initial design criteria for the significant wave height is, $H_s \leq 5\,\mathrm{m}$. This thesis will not go into detail where the possible locations are, but one alternative is at the coast outside West Africa.

Two separate models with different bending stiffness were made. The one model was elastic like a HDPE floater in full scale. The second model were rigid like a steel pipe in full scale. The models will be compared in terms of vertical motion, vertical acceleration, and mooring force. In addition, the models will be compared with the elastic torus and the elastic torus covered with membrane without the skirt. This is done to study the effect off skirt and membrane on the response.

During the experiments, a special attention was made to non-linear effects such as over-topping of waves, out of water and survivability. The results from the experiment will be presented as figures and as a movie from the experiment showing the global behavior of the models. The focus will mainly be on the experimental result from the regular wave test.

A theoretical model of the vertical response for the solar island is developed. The theoretical model is based on the theory for wave-induced vertical motion for circular collar of a floating fish farm (Odd M. Faltinsen, 2012), and the vertical motion for a SES (Odd M Faltinsen, 2005). The theoretical model is made to support the experimental result.

1.3 Outline of the Present Study

This chapter first include the introduction and design of the solar island and then give a review of previous work for floating torus and use of air cushions in marine structures. The objective and structure of the work are outlined afterwards. In Chapter 2 the theory of the waves used in the experiment is presented. The derivation of motion for the torus and vertical motion for the solar island are presented in Chapter 3. Next the experimental set-up, test conditions and the analyzing process is presented in Chapter 4. Then the experimental and numerical results are presented and discussed in Chapter 5. The experimental result will also be presented as a movie that is attached to the report. A conclusion is given in Chapter 6. Finally, a recommendation for further work is given in Chapter 7.

Chapter 2

Theory

From a hydrodynamical point of view it is sufficient to analyze a structure in incident sinusoidal waves of small wave steepness (O. Faltinsen, 1993). The wave steepness is a ratio of wave height divided by the wave length, where small values means linear waves. It is possible to obtain result in irregular seas by linearly superposition from steady state condition. In steady-state conditions the solution oscillates with the incoming wave frequency ω, meaning that it is possible to avoid the time dependence from the problem (Greco, 2016).

2.1 Regular Waves

Regular waves, means waves oscillating in time with period $T = 2\pi/\omega$ and oscillating in space with wavelength $\lambda = 2\pi/k$. The wave profile of regular waves propagating along the x-axis can according to linear theory be written on the form

$$\zeta = \zeta_a \sin(\omega t - kx) \tag{2.1}$$

The wave steepness used in this experiment is found by assuming a significant wave height, $H_s = 5\,\mathrm{m}$ and varying peak period, T_p. By use of the wavenumber and dispersion relation for deep water the steepness can found by Equation (2.2), the result are shown in Table 2.1.

$$H/\lambda = \left(\frac{H_s}{1.56T_p^2}\right)^{-1} \tag{2.2}$$

$\boldsymbol{H_s}$ [m]	$\boldsymbol{T_p}$ [s]	**Steepness**
5	8	20
5	9	25
5	10	30
5	11	40
5	12	45
5	13	50

Table 2.1: The steepness as a function of H_s and T_p.

Linear theory represents a first order approximation in satisfying the free surface conditions. For waves of steepness $H/\lambda = 10$ the exact theory predicts 20 % higher maximum wave elevation than the linear approximation (O. Faltinsen, 1993). The approximation can be improved by a Stoke's expansion, this means introducing higher order terms when satisfying the free surface condition. The second order wave elevation in deep water can be written as (O. Faltinsen, 1993).

$$\zeta_2 = -\frac{1}{2}\zeta_a^2 k \cos[2(\omega t - kx)] \tag{2.3}$$

Combining Equation (2.1) and (2.3) gives the following surface elevation.

$$\zeta = \zeta_a \sin(\omega t - kx) - \frac{1}{2}\zeta_a^2 k \cos[2(\omega t - kx)] \tag{2.4}$$

The second-order solution of the wave elevation sharpens the wave crests and makes the through shallower.

2.2 Irregular Waves

Irregular waves are intended to represent a realistic sea state and are therefore used for studying the actual responses including non-linear phenomena as high frequency and low frequency responses, impact loads and survivability in extreme sea states (Steen, 2014). An irregular short-term sea state can be found by use of superposition of different regular waves with random phase angels. The process is illustrated in Figure 2.1, mathematical it can be written as Equation (2.5).

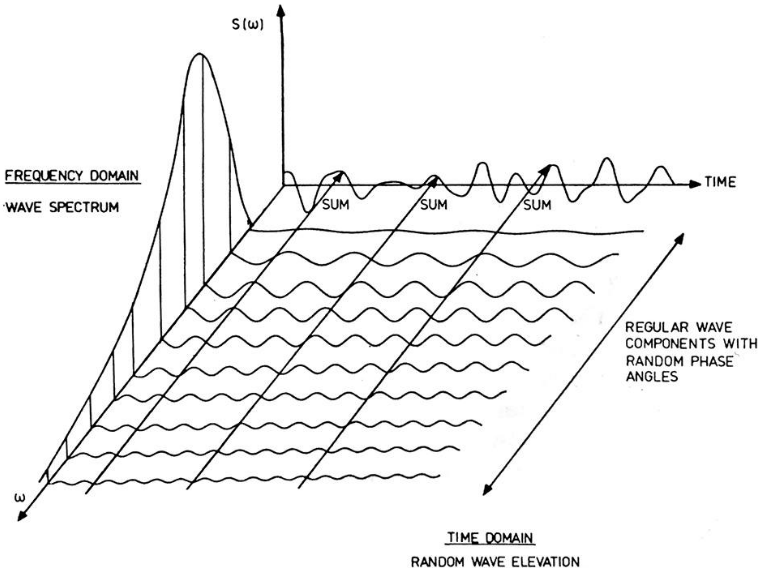

Figure 2.1: Illustration of the superposition principle when creating an irregular sea state. Illustration taken from (O. Faltinsen, 1993).

$$\zeta = \sum_{j=1}^{N} A_j \sin(\omega_j t + \epsilon_j) \tag{2.5}$$

Here A_j is the wave amplitude, ω_j is the angular frequency and ϵ_j is the random phase angle of wave component number j. The random phase angle is uniformly distributed between 0 and 2π and constant with time. The wave amplitude A_j can be expressed by a wave spectrum, $S(\omega)$, as

$$\frac{1}{2}A_j^2 = S(\omega_j)\Delta\omega \tag{2.6}$$

An example of a wave spectrum is the JONSWAP spectrum. The JONSWAP spectrum can be defined as (DNV, 2014)

$$S(\omega) = A_\gamma \frac{5}{16} H_s^2 \omega_p^4 \omega^{-5} \exp\Big(-\frac{5}{4}\big(\frac{\omega}{\omega_p}\big)^{-4}\Big)\gamma^{\exp\Big(-0.5\big(\frac{\omega-\omega_p}{\sigma\omega}\big)^2\Big)} \tag{2.7}$$

Here H_s is the significant wave height. ω_p is the angular spectral peak frequency and is defined as

$$\omega_p = \frac{2\pi}{T_p} \tag{2.8}$$

where T_p is peak period. γ is the non-dimensional peak shape parameter and if no values are given for the peak shape parameter. The following value of γ_p can be applied.

$$\gamma_p = 5 \text{ for } \frac{T_p}{\sqrt{H_s}} \leq 3.6 \tag{2.9}$$

$$\gamma_p = e^{5.75-1.15\frac{T_p}{\sqrt{H_s}}} \text{ for } 3.6 \leq \frac{T_p}{\sqrt{H_s}} < 5 \tag{2.10}$$

$$\gamma_p = 1.0 \text{ for } 5 \leq \frac{T_p}{\sqrt{H_s}} \tag{2.11}$$

σ is the spectral width parameter and can be found as

$$\sigma = \begin{cases} \sigma_a & \text{for } \omega \leq \omega_p \\ \sigma_b & \text{for } \omega > \omega_p \end{cases} \tag{2.12}$$

where typical values are $\sigma_a = 0.07$ and $\sigma_b = 0.09$. A_γ is a normalizing factor, and is given by equation

$$A_{\gamma} = 1 - 0.0287 \ln(\gamma) \tag{2.13}$$

Typical sea state in West Africa with a return period of 100 years are given in Table 2.2, the values are taken from (DNV, 2013). A significant wave height and wave period characterize each sea state. In West Africa and other areas where wind-waves and swell are not collinear the use of double peaked spectrum shall not be applied. Figure 2.2 shows the JONSWAP spectrum for the different areas in West Africa.

West Africa	
Nigeria(swell)	H_s 3.8 m
	T_p 15.0 s
Nigeria (squalls)	H_s 2.5 m
	T_p 7.2 s
Gabon (wind generated)	H_s 2.5 m
	T_p 8.0 s
Gabon (swell)	H_s 4.0 m
	T_p 15.2 s
Ivory Coast (swell)	H_s 6.0 m
	T_p 13.0 s
Mauritania (swell)	H_s 6.1 m
	T_p 19.1 s
Angola (swell, shallow water)	H_s 4.1 m
	T_p 16.0 s

Table 2.2: Typical sea states at different location in West Africa, with a return period of 100 years (DNV, 2013).

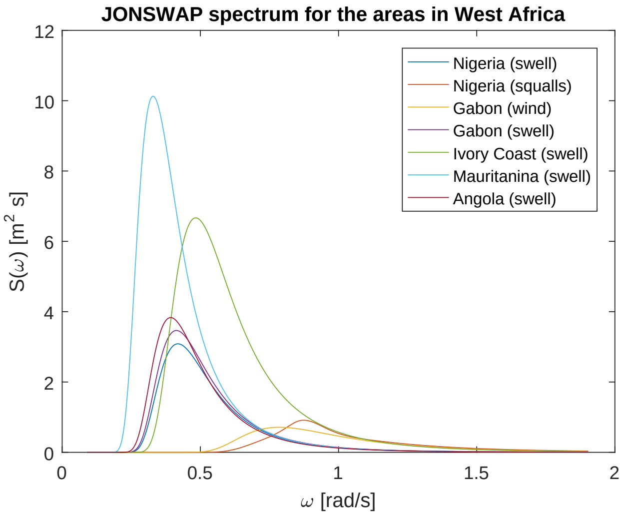

Figure 2.2: The JONSWAP spectrum for the different areas in West Africa given in Table 2.2.

2.3 Wavemaker Theory

Generation of the waves used in the experiment are made by a flap hinged wavemaker that is attached in the student tank at NTNU. The relation between the wave height and the coherent stroke of the wavemaker, H/S can be written as (Dean & Dalrymple, 1991).

$$\frac{H}{S} = f(T, h) \tag{2.14}$$

Where f is the transfer function and is depending on the type of wavemaker, the wave period and the water depth. This means that the desired stroke can be found by.

$$S = \frac{H}{f} \tag{2.15}$$

Hughes (1993) has found the transfer function for a flap hinged distance z from the surface to be

$$f = \frac{4\sinh(kh)}{\sinh(2kh) + 2kh} \cdot \frac{\sinh(kh) + \cosh(kh - kz) - \cosh(kh)}{kz} \tag{2.16}$$

Where h is the water depth, and k is the wave number. For the irregular sea state the desired stroke can be written as the following sum

$$S(t) = \sum_{j=1}^{\infty} \frac{2\sqrt{2(S(\omega_j)\Delta\omega}}{f(\omega_j)} sin(\omega_j t + \epsilon_j) \tag{2.17}$$

2.4 Scaling Laws

To achieve similarity in forces between model scale and full scale, the following conditions must be fulfilled; geometrical similarity, kinematic similarity, and dynamic similarity. Since the problem is hydroelastic, additional requirements are needed. The additional requirements are; correctly scaled global structural stiffness, structural damping must be like full scale values and the mass distribution must be similar (Steen, 2014).

The incident waves are gravity driven and therefore Froude scaling must be used. Equality in Froude number, geometrical and kinematic similarity will ensure similarity between inertia and gravity forces. Using the geometrical similarity requirement gives the scaling ratio $\lambda = L_F/L_M$. Table 2.3 shows how to scale different physical parameters.

Since Froude scaling is used, Reynolds number scaling cannot be satisfied. Equality in Reynolds number will ensure that the viscous force is correctly scaled. Without flow separation viscous effects are associated with the boundary layer flow and negligible relative to potential-flow effects (Li et al., 2014).

Physical Parameter	**Unit**	**Multiplication factor**
Length	[m]	λ
Structural mass	[kg]	$\lambda^3 \rho_F / \rho_M$
Force	[N]	$\lambda^3 \rho_F / \rho_M$
Acceleration	[m/s^2]	$a_F = a_M$
Time	[s]	$\sqrt{\lambda}$
Pressure	[Pa]	$\lambda \rho_F / \rho_M$
Velocity	[m/s]	λ
Bending stiffness	[Nm^2]	λ^5

Table 2.3: Froude scaling table for different physical parameters used in the experiment.

Chapter 3

Theoretical Model of the Response

The theoretical vertical response of the solar island will be investigated in deep water linear waves. The island is freely floating without the presence of mooring system and zero current. Any coupling between horizontal and vertical motion will be neglected. Due to the assumption of linearity the superposition principle is valid and the vertical motion of the floater and air cushion can be solved separately.

A Cartesian coordinate system (x,y,z) is defined, were the z- axis is the torus axis and upwards, with the mean free surface at z = 0. The incident wave velocity potential for linear waves propagating along the x-axis is expressed as

$$\phi_0 = \frac{g\zeta_a}{\omega} \exp(\nu z + i\nu x - i\omega t) \tag{3.1}$$

Here i is a complex number with the property $\sqrt{i} = -1$. ζ_a is the wave amplitude, g is the acceleration of gravity and the wavenumber $\nu = \omega^2/g$. A complex expression is used to simplify the calculations, but it is only the real part that has physical meaning. The considered incident wave length are assumed large relative to the cross-sectional torus radius, which means that the wave scattering and radiation by the torus can be neglected. The wave elevation can be found by using the dynamic Equation (3.2) (O. Faltinsen, 1993).

$$g\zeta + \frac{\partial \phi}{\partial t} = 0 \text{ on } z = 0 \tag{3.2}$$

Hence the wave elevation ζ is

$$\zeta = i\zeta_a \exp(i\nu x - \omega t) \tag{3.3}$$

3.1 Heave Motion for the Air Cushion

The heave motion for the air cushion is based on the theory from the book given in the References as Odd M Faltinsen (2005). During the derivation, the pressure is assumed constant in the whole air cushion, and the pitch motion is neglected. The continuity equation for the air mass inside the cushion can be written as

$$\rho_a Q_{in} - \rho_a Q_{out} = \frac{d}{dt}(\rho_c \Omega) \tag{3.4}$$

Here ρ_a is the air mass density at equilibrium pressure. $\rho_a Q_{in}$ is the air mass flow per unit time through the fans. $\rho_a Q_{out}$ is the air mass flow per unit time due to leakage. ρ_c is the dynamic air mass density of the pressurized air cushion. Ω is the air cushion volume. Assuming that there is no in- and out-flow Equation (3.4) becomes.

$$\frac{d}{dt}(\rho_c \Omega) = 0 \tag{3.5}$$

Equation (3.5) can be linearized as

$$\frac{d}{dt}(\rho_c \Omega) \sim \frac{d\rho_c}{dt} A_b h_b + \rho_a \frac{d\Omega}{dt} \tag{3.6}$$

where A_b is the cushion area and h_b is the cushion plenum height, see Figure 3.1.

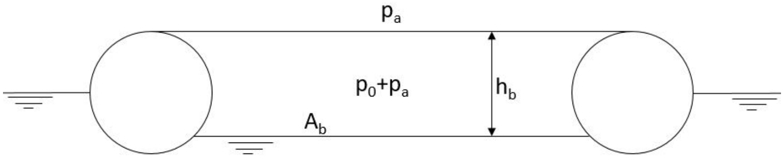

Figure 3.1: Transverse cross-section of the solar island. A_b is the cushion area, h_b is the cushion plenum height, p_a is the atmospheric pressure and p_0 is the excess pressure.

The relationship between the pressure and mass density is based on the adiabatic condition given in Equation (3.7).

$$\frac{p}{p_0 + p_a} = \left(\frac{\rho_c}{\rho_a}\right)^{\gamma} \tag{3.7}$$

Here γ is the ratio of specific heat for air, and is equal 1.4. p_0 is the excess pressure in the cushion and p_a is the atmospheric pressure. The total pressure inside the air cushion is given by Equation (3.8)

$$p = p_0 + \mu(t)p_0 \tag{3.8}$$

where $p_0\mu(t)$ is the dynamic part of the pressure. The total pressure does not include the atmospheric pressure since it is on both sides of the cushion. The cushion plenum height can be found for a given pressure by

$$h_b = \frac{p_0}{\rho g} \tag{3.9}$$

Equation (3.7) can be linearized as

$$\frac{\rho_c}{\rho_a} \sim \left(1 + \frac{1}{\gamma}\mu(t)\right) \tag{3.10}$$

By use of Equation (3.10) $d\rho_c/dt$ can be expressed as

$$\frac{d\rho_c}{dt} = \frac{\rho_a}{\gamma}\frac{d\mu}{dt} \tag{3.11}$$

The volume of the air cushion will change due to heave and wave motions. The change can be expressed as

$$\frac{d\Omega}{dt} = A_b\frac{d\eta_3}{dt} + \frac{dV_W}{dt} \tag{3.12}$$

where dV_w/dt is associated with the wave motion and is expressed as

$$\frac{dV_w}{dt} = \iint_R \frac{d\zeta}{dt}dxdy \tag{3.13}$$

By differentiation of Equation (3.3) with respect to time, and converting the integral to polar coordinates Equation (3.13) becomes

$$\frac{dV_w}{dt} = -\omega\zeta_a e^{-i\omega t}\int_0^{2\pi}\int_0^R e^{i\nu rcos(\theta)}rdrd\theta \tag{3.14}$$

The integral in Equation (3.14) are solved by numerical integration in Matlab.

$$q = \int_0^{2\pi}\int_0^R e^{i\nu rcos(\theta)}rdrd\theta \tag{3.15}$$

$$\frac{dV_w}{dt} = -\omega\zeta_a q e^{-i\omega t} \tag{3.16}$$

Hence V_w can be written as

$$V_w = -iq\zeta_a e^{-i\omega t} \tag{3.17}$$

Inserting Equation (3.11) and (3.12) into Equation (3.6) the following equation arise

$$\frac{\rho_a}{\gamma}\frac{d\mu}{dt}A_b h_b + \rho_a(A_b\frac{d\eta_3}{dt} + \frac{dV_W}{dt}) = 0 \tag{3.18}$$

μ can be eliminate from equation (3.18) by Newton's second law

$$M\frac{d^2\eta_3}{dt^2} = p_0\mu(t)A_b \tag{3.19}$$

Here M is the mass of the island. Equation (3.19) are only considering the forces due to the dynamic excess pressure, this means that the hydrodynamic forces on the torus are neglected. Equation (3.18) then becomes

$$\frac{\rho_a}{\gamma}\frac{1}{p_0}\frac{M}{h_b}\frac{d^3\eta_3}{dt} + \rho_a(A_b\frac{d\eta_3}{dt} + \frac{dV_W}{dt}) = 0 \tag{3.20}$$

This is a third-order differential equation in η_3. Assuming a steady-state solution the integration of equation (3.20) once with respect to time becomes

$$\frac{Mh_b}{\gamma(p_0)}\frac{d^2\eta_3}{dt^2} + A_b\eta_3 = -V_w \tag{3.21}$$

By rearranging Equation (3.21), the differential equation for the heave motion becomes

$$M\frac{d^2\eta_3}{dt^2} + \frac{A_b\gamma p_0}{h_b}\eta_3 = -\frac{\gamma p_0}{h_b}V_w \tag{3.22}$$

3.2 Heave Motion for the Torus

The presented derivation for the vertical motion of the torus is taken from the articles given in the References as Odd M. Faltinsen (2012) and Li (2017). The vertical motion is found by matching asymptotic expansion with a far- and near-field solution. The floater is assumed to be semi-submerged in water of infinite depth and horizontal extent.

The problem is considered in the limiting case that the forcing frequency $\omega \to 0$, which means that a rigid free-surface condition can be used (Odd M. Faltinsen, 2011). The rigid free surface condition can mathematical be written as Equation (3.23), and means that no waves are generated i.e. zero damping.

$$\frac{\partial \phi}{\partial z} = 0 \text{ on } z = 0 \tag{3.23}$$

As mention in the literature review a theory valid for the classical linear free-surface has been developed. A comparison between the frequency-dependent and zero frequency theory for the response amplitude operator (RAO) is done by Peng Li [Li, Personal communication (2017)]. The result for heave are shown in Figure 3.2, and pitch in Figure 3.3. The results shows that there are little difference in the frequency of interest. Therefor the zero frequency theory is used due to simplicity.

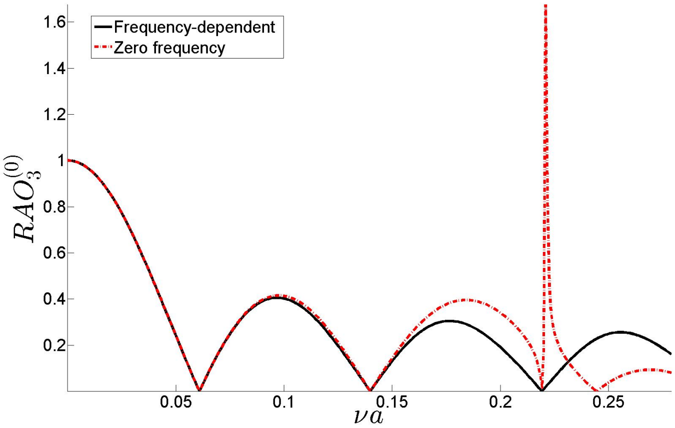

Figure 3.2: Comparison between the RAO in heave for the frequency-dependent and zero frequency theory. The results are plotted against the non dimensional wavenumber. The calculations are done by Peng Li [Li, Personal communication (2017)].

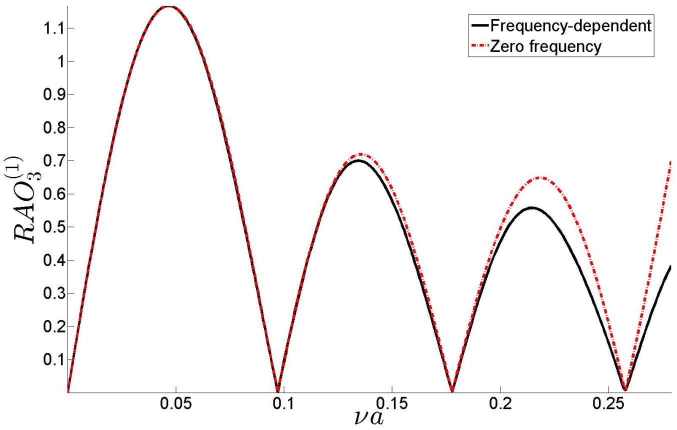

Figure 3.3: Comparison between the RAO in pitch for the frequency-dependent and zero frequency theory. The results are plotted against the non dimensional wavenumber. The calculations are done by Peng Li [Li, Personal communication (2017)].

3.2.1 Far-Field Flow Description

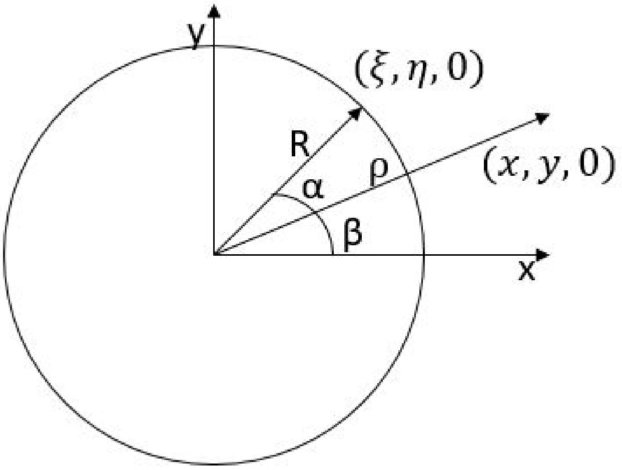

Figure 3.4: Far-field view of the torus with parameter and coordinate definitions.

Figure 3.4 is showing the far-field view of the torus. In the far-field the flow will appear as a line distribution of sources with constant density Q, along the center line of the torus. This is because the details of the cross-dimension is not seen in the far-field. The velocity potential at any point P, due to a three-dimensional point source, in a liquid at rest at infinity is (O. Faltinsen, 1993).

$$\phi = \frac{Q}{4\pi r} \tag{3.24}$$

Here r is the radial distance from the point (x, y, z) to a point at the center line of the torus $(\xi, \eta, 0)$. Q is the source strength. The coordinates of the center line can be expressed as in Equation (3.25), while the field point expression is shown in Equation (3.26).

$$\xi = R\cos\alpha, \eta = R\sin\alpha, \zeta = 0 \tag{3.25}$$

$$x = \rho\cos\beta, y = \rho\sin\beta, z = 0 \tag{3.26}$$

The radial distance can thus be written as

$$r = \sqrt{x^2 - 2xR\cos(\alpha) + y^2 - 2yR\sin(\alpha) + R^2 + z^2} \tag{3.27}$$

The far-field velocity potential is found by integrating the expression for a source point around the floater with respect to the angel α. The expression becomes the following

$$\phi^F = \frac{QR}{4\pi}\int_0^{2\pi} \frac{d\alpha}{\sqrt{x^2 - 2xR\cos(\alpha) + y^2 - 2yR\sin(\alpha) + R^2 + z^2}} \tag{3.28}$$

The integral in Equation (3.28) can be simplified by introducing the angle $\alpha_1 = \alpha - \beta$, and use the fact that the radial distance can be written as $r = \sqrt{(\rho - R)^2 + z^2}$. The simplification leads to the following.

$$\phi^F = \frac{QR}{4\pi}\int_0^{2\pi}\frac{d\alpha_1}{\sqrt{r^2+2\rho R(1-cos(\alpha_1))}} = \frac{QR}{\pi\sqrt{r^2+4\rho R}}K\left(2\sqrt{\frac{\rho R}{r^2+4\rho R}}\right) \tag{3.29}$$

Here $K()$ is the Elliptic K-function defined in Maple. A first-term inner expansion of the far-filed expression is

$$\phi_I^F = \frac{Q}{2\pi}\ln(\frac{8R}{r}) \tag{3.30}$$

3.2.2 Near-Field Flow Description

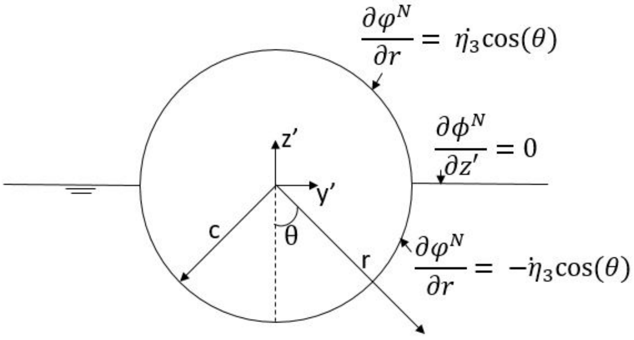

Figure 3.5: Near-field view of the cross-section of a torus. With local coordinate system and boundary conditions for the near filed solution of the velocity potential.

Figure 3.5 is showing the near-field view of the torus, with a local coordinate system. The local coordinate system has origin in the center of the circle. The following relationship is assumed $y' = c\sin(\theta), z' = c\cos(\theta)$ with $\theta = 0$ corresponding to the negative z'-axis. The draught is assumed to be equal to the radius of the cross section, c. The cross section is split into two semicircles defined by $-\pi/2 < 0 < \pi/2$ and $\pi/2 < 0 < 3\pi/2$. In heave, the two semicircles are heaving with opposite signs. A consequence of the formulation is that the flow will be symmetric about the y-axis, meaning no vertical flow at $z' = 0$, thus the rigid free surface condition is satisfied. A complete near field solution of the velocity can now be expressed as

$$\phi^N = \dot{\eta}_3 \big(C \ln \big(\frac{r}{R} \big) + A_0 + \sum_{n=1}^{\infty} A_n \frac{cos(n\theta)}{r^n} \big) \tag{3.31}$$

Here $\dot{\eta}_3$ is the heave velocity. The constants C and A_n, $n = 0, ..\infty$ are determined by matching with the far-field solution and by the body-boundary conditions. The body-boundary conditions are

$$\frac{\partial \phi^N}{\partial r}|_{r=c} = \begin{cases} -\dot{\eta}_3 \cos(\theta) & -\pi/2 < \theta < \pi/2 \\ \dot{\eta}_3 \cos(\theta) & -\pi < \theta < -\pi/2 \text{ and } \pi/2 < \theta < \pi \end{cases} \tag{3.32}$$

The constant C is found by integrating the boundary condition from $\theta = -\pi$ to π, and it's found to be

$$C = -2c/\pi \tag{3.33}$$

The A_n coefficients can be found by multiplying the body-boundary condition with $\cos(n\theta)$ and integrating from $\theta = -\pi$ to π the equation becomes

$$-nA_n \frac{\pi}{c^{n+1}} = -\int_{-\pi/2}^{\pi/2} \cos(\theta)\cos(n\theta) d\theta + \int_{3\pi/2}^{\pi/2} \cos(\theta)\cos(n\theta) = \frac{3\cos\left(\frac{n\pi}{2}\right) + \cos\left(\frac{3n\pi}{2}\right)}{n^2 - 1} \tag{3.34}$$

The right-hand side is zero for odd numbers, the non-zero coefficients are given by

$$A_{2m} = -c^{2m+1} \frac{3\cos(m\pi) + cos(3m\pi)}{\pi 2m(4m^2 - 1)}, m = 1, .. \tag{3.35}$$

Equation (3.31) can now be expressed as

$$\phi^N = \dot{\eta}_3\Big(C\ln\big(\frac{r}{R}\big) + A_0 + \sum_{m=1}^{\infty} A_{2m}\frac{\cos(2m\theta)}{r^{2m}}\Big) \tag{3.36}$$

The last constant, A_0, must be found by matching the outer expansion of the near-filed velocity potential, Equation (3.36), with the inner expansion of the far-field velocity potential, Equation (3.30). Mathematical this means

$$\phi_I^F = \phi^N_{r\to\infty} \tag{3.37}$$

$$-\frac{Q}{2\pi}\ln\big(\frac{r}{R}\big) + \frac{Q}{2\pi}\ln(8) = \dot{\eta}_3 C\ln\big(\frac{r}{R}\big) + \dot{\eta}_3 A_0 \tag{3.38}$$

Solving Equation (3.38) gives the value for A_0 to be

$$A_0 = -C\ln 8 \tag{3.39}$$

$$-\dot{\eta}_3 = \frac{Q}{2\pi} \tag{3.40}$$

3.2.3 Heave Added Mass

The added mass in heave is found by considering forced harmonic motion of the structure. This will lead to a force on the structure, where the linear part is written as

$$F_3 = -A_{33}\ddot{\eta}_3 \tag{3.41}$$

The force is obtained by integrate the linear dynamic pressure $p = -\rho\partial\phi^N/\partial t$ multiplied with minus the z'-component $\cos(\theta)$ over the submerged hull surface. Hence it follows that added mass in heave A_{33} is.

$$\begin{aligned} A_{33} &= \rho 2\pi Rc \int_{-\pi/2}^{\pi/2} \Big(C \ln\big(\frac{c}{R}\big) + A_0 + \sum_{m=1}^{\infty} A_{2m} \frac{\cos(2m\theta)}{c^{2m}} \Big) \cos(\theta) d\theta \\ &= \frac{4M}{\pi} \left[\frac{2}{\pi} \ln(\frac{8R}{c}) + \underbrace{\sum_{m=1}^{\infty} \frac{(3\cos(m\pi) + \cos(3m\pi)\cos(m\pi))}{\pi 2m(4m^2-1)^2}}_{0.07238725793} \right] \end{aligned} \tag{3.42}$$

Here $M = \rho\pi^2 Rc^2$ is the mass of the displaced water by the torus. The two-dimensional added mass in heave can be found by

$$a_{33} = \frac{A_{33}}{2\pi R} \tag{3.43}$$

3.2.4 Vertical Excitation Force

Due to linearity, the superposition principle is valid and the velocity potential, ϕ, can be decomposed in terms of the fundamental physical effects involved in the fluid-body interaction (Greco, 2016). The vertical wave excitation is divided into a Froude-Kriloff part and a diffraction part. The Froude-Kriloff force is due to the undisturbed dynamic pressure from the incident waves. The expression for the dynamic pressure is

$$p_{dyn} = -\rho \frac{\partial \phi_0}{\partial t} = i\rho g \zeta_a \exp(\nu z + i\nu x - i\omega t) \text{ , where } x = R\cos(\beta) \tag{3.44}$$

Using the identity found in Abramowitz and Stegun (1964) we can write.

$$\exp(i\nu R\cos(\beta)) = J_0(\nu R) + \sum_{m=1}^{\infty} 2i^m J_m(\nu R) \cos m\beta \tag{3.45}$$

Here $J_0(\nu R)$ and $J_n(\nu R)$ are Bessel functions of the first kind with order 0 and n respectively. The Froude-Kriloff force are obtained by integrating the incident wave pressure along the mean wetted surface.

$$f_3^{FK} = -\int_{S_{0,B}} p_{dyn}\eta_3 dS = -\int_{-\pi/2}^{\pi/2} p_{dyn}\cos(\theta) c d\theta \tag{3.46}$$

$$f_3^{FK} = \rho g \zeta_a i[J_0(\nu R) + \sum_{m=1}^{\infty} 2i^m J_m(\nu R)\cos m\beta] b_w \exp(-i\omega t) \tag{3.47}$$

Here $b_w = 2c$. The presence of the body in the fluid results in diffraction of the incident wave system (J. N. Newman, 1977a). The diffraction problem involves solving a boundary value problem with forced oscillations with minus the incident vertical velocity along the floater. As a consequence the diffraction force per unit length are

$$f_3^D = a_z a_{33} + u b_{33} \tag{3.48}$$

Here a_z and u are the vertical particle acceleration and velocity of the incident waves. Due to the assumption that the wave length are large relative to the cross-sectional radius means that the damping contribution b_{33} can be neglected. The vertical particle acceleration can be found by Equation (3.49).

$$a_z = \frac{\partial^2 \phi_0}{\partial z \partial t} = -i\omega^2 \zeta_a \exp(\nu z_m + i\nu x - i\omega t) \tag{3.49}$$

Here z_m is a weighted z-coordinate of the floater and will be set equal to zero. This approximation holds for long waves since the variation of the vertical acceleration with depth will be smaller the longer the waves are. The vertical diffraction force per unit length then becomes

$$f_3^D = -i\omega^2 \zeta_a [J_0(\nu R) a_{33} + \sum_{m=1}^{\infty} 2i^m J_m(\nu R) a_{33}^m \cos(m\beta)] \exp(-i\omega t) \tag{3.50}$$

Here a_{33} is given by Equation (3.43). a_{33}^m is the 2D added mass for the different modes.

3.2.5 Vertical Motions

The vertical motion of the torus is assumed to follow the beam equation

$$m\frac{\partial^2 w}{\partial t^2} + \rho g b_w + EI\frac{\partial^4 w}{\partial s^4} = f_3^{added\ mass} + f_3^{wave\ excit} \tag{3.51}$$

Here m is the torus mass per unit length, EI is the bending stiffness and the differentiation $\partial/\partial s$ is along the torus. $f_3^{added\ mass}$ is the vertical added mass force per unit length of the torus, and $f_3^{wave\ excit}$ is the vertical wave excitation force on the floater per unit length. Further ρ is the mass density of water. The vertical motion of the torus, w is expressed as the following Fourier series

$$w = a_0(t) + \sum_{n=1}^{\infty} a_n(t)\cos(n\beta) \tag{3.52}$$

If rigid-body motion are considered, $a_0(t)$ and $a_1(t)$ represent heave and pitch. By substitute Equation (3.52) into equation (3.51), and use that $\partial/\partial s = R^{-1}\partial/\partial\beta$. The resulting equation are then multiplied successively by $\cos(n\beta)$, n = 0,1,.. and integrate from $\beta = 0$ to 2π. Utilization of the property of orthogonal functions, shown in Equation (3.53), the modal differential equation for the first mode, (n = 0, heave), are shown in Equation (3.54).

$$\int_0^{2\pi} \cos n\beta \cos m\beta d\beta \begin{cases} = 0, & n \neq m \\ = 2\pi, & n = m = 0 \\ = \pi, & n = m = \ 1, 2, .. \end{cases} \tag{3.53}$$

$$\big(m + a_{33}\big)\frac{d^2\eta_3}{dt^2} + \rho g b_w \eta_3 = \big(\rho g b_w - \omega^2 a_{33}\big)\zeta_a J_0(\nu R) i e^{-i\omega t} \tag{3.54}$$

3.3 The Heave Equation for the Floating Solar Island

Equation (3.54) is per unit length of the torus. So in order to add Equation (3.22) and (3.54), the terms in Equation (3.54) must be multiplied with $2\pi R$ in order to get the same dimensions. This leads to the following differential equation to describe the heave motion for the solar island.

$$\begin{aligned}\frac{d^2\eta_3}{dt^2}\Big(2\pi R(m+a_{33})+M\Big)+\Big(2\pi R\rho g b_w+\frac{A_b\gamma p_0}{h_b}\Big)\eta_3 &= \frac{\gamma p_0}{h_b}i\zeta_a q e^{-i\omega t}\\ &+2\pi R\big(\rho g b_w-\omega^2 a_{33}\big)\zeta_a J_0(\nu R)ie^{-i\omega t}\end{aligned} \tag{3.55}$$

In order to solve equation (3.55) the solution of η_3 is assumed to be harmonic with the same circular frequency ω as the incident waves i.e. steady state.

$$\eta_3=\eta_{3a}e^{-i\omega t} \tag{3.56}$$

Equation (3.56) are substituted into Equation (3.55) and solved with respect to η_{3a}. The expression becomes

$$\eta_{3a}=\frac{2\pi R\big(\rho g b_w-\omega^2 a_{33}\big)\zeta_a J_0(\nu R)i+\frac{\gamma p_0}{h_b}i\zeta_a q}{-\omega^2\Big(2\pi R(m+a_{33})+M\Big)+\Big(2\pi R\rho g b_w+\frac{A_b\gamma p_0}{h_b}\Big)} \tag{3.57}$$

The linear transfer function for the heave motion is obtained by taking the absolute value of η_{3a}/ζ_a. The transfer functions, giving the normalized response amplitude for each wave circular frequency are

$$\left|\frac{\eta_{3a}}{\zeta_a}\right|=\left|\frac{2\pi R\big(\rho g b_w-\omega^2 a_{33}^{(0)}\big)J_0(\nu R)i+\frac{\gamma p_0}{h_b}iq}{-\omega^2\Big(2\pi R(m+a_{33}^{(0)})+M\Big)+\Big(2\pi R\rho g b_w+\frac{A_b\gamma p_0}{h_b}\Big)}\right| \tag{3.58}$$

The linear transfer function for the torus can be found by substitute Equation (3.56) into Equation (3.54). The equation is solved with respect to η_{3a} and divided by the wave amplitude. The transfer function in heave for the torus, giving the normalized response amplitude for each wave circular frequency are

$$\left|\frac{\eta_{3a}}{\zeta_a}\right| = \left|\frac{\big(\rho g b_w - \omega^2 a_{33}^{(0)}\big) J_0(\nu R) i}{-\omega^2\Big(m + a_{33}^{(0)}\Big) + \rho g b_w}\right| \tag{3.59}$$

3.4 The Pitch Equation for the Torus

The pitch motion of the structure can be written as

$$a_1 = \eta_5 R \tag{3.60}$$

The model differential equation for the pitch motion are found by use of Equation (3.51), with n = 1 pitch. Hence the equation becomes

$$\big(m + a_{33}^{(1)}\big)\frac{d^2 a_1}{dt^2} + (\rho g b_w + n^4\frac{EI}{R^4})a_1 = \big(\rho g b_w - \omega^2 a_{33}^{(1)}\big)\zeta_a 2 J_1(\nu R) i e^{-i\omega t} \tag{3.61}$$

Here $a_{33}^{(1)}$ is the generalized added mass coefficient for the pitch motion. The generalized added mass coefficient is found in a similar procedure as described for the heave motion. The vertical velocity of the torus can be expressed as

$$\dot{w} = \dot{a}_0 + \sum_{n=1}^{\infty} \dot{a}_n \cos(n\beta) \tag{3.62}$$

The general far filed velocity potential associated with the general mode $\cos(n\beta)$ can now be expressed as

$$\phi_n^F = \frac{QR}{4\pi}\int_0^{2\pi}\frac{\cos(n\alpha)d\alpha}{\sqrt{r^2+2aR[1-\cos(\alpha-\beta)]}} \tag{3.63}$$

Introducing $\alpha_1 = \alpha - \beta$ the expression can be rewritten as the following,

$$\phi_n^F = \frac{QR}{4\pi}\cos(n\beta)\int_0^{2\pi}\frac{\cos n\alpha_1 d\alpha_1}{\sqrt{r^2+2aR[1-cos(\alpha_1)]}} \tag{3.64}$$

A first term inner expansion of ϕ_I^F will lead to the following expression for different n-values.

$$\phi_I^F = \frac{Q\cos(n\beta)}{2\pi}\Big[-K_n + \ln(\frac{8R}{r})\Big] \tag{3.65}$$

Where K_n is defined for any n as

$$K_n = \frac{1}{2\sqrt{2}}\int_0^{2\pi}\frac{1-\cos(nx)dx}{\sqrt{1-\cos(x)}} \tag{3.66}$$

Then $K_1 = 2$. The general near-field expression can now be written as

$$\phi^N = \dot{a}_n\cos(n\beta)\big(C\ln\big(\frac{r}{R}\big) + C_n + A_0 + \sum_{n=1}^{\infty}A_n\frac{\cos(n\theta)}{r^n}\big) \tag{3.67}$$

Here $\dot{a}_3\cos(n\beta)$ are the vertical velocity. The constants C and A_n, $n = 0, ..\infty$ are determined by matching with the far-field solution and by the body-boundary conditions. The body-boundary conditions are

$$\frac{\partial\phi^N}{\partial r}|_{r=c} = \begin{cases} -\dot{a}_n\cos(n\beta)\cos(\theta) & -\pi/2 < \theta < \pi/2 \\ \dot{a}_n\cos(n\beta)\cos(\theta) & -\pi < \theta < -\pi/2 \text{ and } \pi/2 < \theta < \pi \end{cases} \tag{3.68}$$

The constant A_0 is found in Equation (3.39). C is the value in Equation (3.33) and A_n is found in Equation (3.35). C_n is determined by matched asymptotic expansion of the general far- and near-filed velocity potential. Mathematical this means

$$\phi_{nI}^{F} = \phi_{nr\rightarrow\infty}^{N} \tag{3.69}$$

$$\frac{Q}{2\pi}\cos(n\beta)\Big[\ln 8 - \ln(\frac{r}{R} - K_n)\Big] = \dot{a}_n \cos(n\beta)\Big[C_n - \frac{2c}{\pi}\ln(\frac{r}{R})\Big] \tag{3.70}$$

Solving the equation with respect to $\dot{a}_n$ and C_n, the general velocity becomes $\dot{a}_n = Q/4c$ and

$$C_n = \frac{2c}{\pi}(\ln 8 - K_n) \tag{3.71}$$

The expression for the near field potential for a general vertical velocity $\dot{a}_n\cos(n\beta)$ on the surface of the torus becomes

$$\phi_n^N = \dot{a}_n\cos(n\beta)\left\{\frac{2c}{\pi}\big[\ln(\frac{(8R)}{c}) - K_n\big] - \sum_{m=1}^{\infty} A_{2m}\frac{\cos(2m\theta)}{c^{2m}}\right\} \tag{3.72}$$

The generalized added mass for the vertical mode can now be found in the same way as described above

$$a_{33}^{(n)} = -\rho\int_{-\pi/2}^{\pi/2}\left[\frac{2c}{\pi}\left\{\ln(\frac{8R}{c} - K_n)\right\} - c\sum_{m=1}^{\infty}\frac{3\cos(m\pi) + \cos(3m\pi)}{2\pi m(4m^2-1)}\cos(2m\theta)\right] \cos(\theta)cd\theta \tag{3.73}$$

Solving the integral gives the following result

$$a_{33}^{(n)} = 2\rho c^2 \left\{ \frac{2}{\pi} \left[\ln(\frac{8R}{c}) - K_n \right] + 0.07238725793 \right\} \tag{3.74}$$

The linear transfer function for the pitch motion of the torus can be found by substitute $a_1 = a_{1a} \exp(-i\omega t)$ into Equation (3.61). The equation is solved with respect to a_1 and divided by the wave amplitude.

$$\left| \frac{a_{1a}}{\zeta_a} \right| = \left| \frac{\left(\rho g b_w - \omega^2 a_{33}^{(1)}\right) J_1(\nu R) 2 i^2}{-\omega^2 \left(m + a_{33}^{(1)}\right) + \rho g b_w + \frac{EI}{R^4}} \right| \tag{3.75}$$

The membrane covering the torus will give a contribution to the force. The force contribution is calculated in the same manner as for heave. The difference is that the integral in Equation (3.14) is multiplied with the arm $r\cos(\theta)$

$$\frac{dV_w}{dt} = -\omega \zeta_a e^{-i\omega t} \int_0^{2\pi} \int_0^R e^{i\nu r cos(\theta)} r^2 \cos(\theta) dr d\theta \tag{3.76}$$

The linear transfer function for the pitch motion of the island can then be written as

$$\left| \frac{a_{1a}}{\zeta_a} \right| = \left| \frac{\left[\left(\rho g b_w - \omega^2 a_{33}^{(1)}\right) J_1(\nu R) 2 i^2\right] 2\pi R + \frac{\gamma p_0}{h_b} V_w}{\left[- \omega^2 \left(m + a_{33}^{(1)}\right) + \rho g b_w + \frac{EI}{R^4}\right] 2\pi R} \right| \tag{3.77}$$

3.5 Horizontal Motions of the Torus

The horizontal acceleration of the torus can be found by use of Newton's second law

$$M \ddot{\eta}_1 = F_{\text{wave exc}} + F_{\text{mooring}} \tag{3.78}$$

Here $\ddot{\eta}_1$ is the acceleration in surge. $F_{\text{wave exc}}$ is the lateral wave excitation loads on the floater. F_{mooring} is the mooring force. The radial wave excitation force per unit length on the floater can found by

$$f_1^{\text{wave exc}} = (\rho A + a_{11}) a_\beta \tag{3.79}$$

Here $A = 0.5\pi c^2$, a_{11} is the two-dimensional added mass for the lateral motion. Use of strip theory the two-dimensional added mass for lateral motions can be expressed as (Odd M. Faltinsen, 2012)

$$a_{11} = \rho \frac{\pi}{2} c^2 \tag{3.80}$$

a_β is the radial incident wave acceleration in the radial direction of the floater, and can be found derivation of the incident wave potential given in Equation (3.1).

$$a_\beta = \frac{\partial^2 \phi}{\partial t \partial x} \cos(\beta) = \omega^2 \zeta_a \exp(i\nu x - i\omega t) \cos(\beta) \tag{3.81}$$

By use of the relation shown in Equation (3.45) the radial wave excitation force per unit length can be written as

$$\begin{aligned} f_1^{\text{wave exc}} =& (\rho A + a_{11}) \omega^2 \zeta_a \exp(-i\omega t) \\ & \cdot \left[J_0(\nu R) \cos(\beta) + \sum_{m=1}^{\infty} i^m J_m(\nu R) \{ \cos[(m-1)\beta] + \cos[(m+1)\beta] \} \right] \end{aligned} \tag{3.82}$$

The lateral wave excitation force can then be found by

$$f_1 = \int_0^{2\pi} f_1^{\text{wave exc}} \cos(\beta) d\beta \tag{3.83}$$

Solving the integral leads to the following force per unit length of the torus

$$f_1 = \pi 2 a_{11} \omega^2 \zeta_a \big[(J_2(\nu R) - J_0(\nu R) \big] \exp(-i\omega t) \tag{3.84}$$

The force from the wave excitation are then found by multiplying Equation (3.84) with $2\pi R$. The mooring force will create a restoring term that is dependent on the spring stiffness for the mooring lines. The restoring term is proportional with the surge motion. Equation (3.78) can now be written as

$$(M + A_{11})\ddot{\eta}_1 - C\eta_1 = F_1 \tag{3.85}$$

Here C is the equivalent stiffness, k_{eq}, in x-direction from all the of moorings used in the experiment. The assumption of steady state leads to the flowing amplitude of the surge motion

$$\left| \eta_{1a} \right| = \left| \frac{F_1}{\omega^2 (M + A_{11}) + C} \right| \tag{3.86}$$

The force in the mooring lines can then be estimated by

$$\hat{F} = k_s \eta_{1a} \tag{3.87}$$

Here k_s is the spring stiffness in x-direction used in the experiment. The natural frequency in surge can be found by

$$\omega_0 = \sqrt{\frac{k}{m}} = \sqrt{\frac{k_{eq}}{M + A_{11}}} \tag{3.88}$$

Chapter 4

Model Tests

Investigation of the behavior for the solar island in waves and current has been done through model testing. One elastic and one rigid model were made of the solar island with Froude scaling 1:50, the main dimensions for the model are given in Table 4.1. In addition, regular wave test of the elastic torus with and without skirt and membrane were performed.

The models were tested at the student model tank at NTNU. The tank is 25 m long, 2.5 m wide and 1.2 m deep. It is equipped with a towing carriage, a flap-piston wave maker and a diagonal damping beach. The current was simulated by towing the model with constant forward speed.

The sampling frequency was 100 Hz, all sensors were calibrated before measurement.

Description	**Mod scale flexible**	**F scale flexible**	**Mod scale Rigid**	**F scale rigid**
Torus diameter	1 m	50 m	1 m	50 m
Cross-sectional diameter	31 mm	1.55 m	27 mm	1.35 m
Skirt length	7 cm	3.5 m	7 cm	3.5 m
Weighted ballast	6.2 g	794 kg	6.2 g	794 kg
PV	145 g	18578 kg	145 g	18578 kg
Spring stiffness	17 N/m	-	17 N/m	-
Pre-tension	2 N	-	2 N	-

Table 4.1: Dimensions in the model tests. Froude scale 1:50.

4.1 Experimental Set-up

The experimental set-up of the model are illustrated in Figure 4.1. The exact same setup is used for both models. The model was attached to the carriage in the middle of the tank by means of four identical nearly horizontal mooring lines, at position 45, 135, 225 and 315 degrees from the center of the circle. Springs with stiffness $k_s = 17\,\mathrm{N/m}$, with a pre-tension $T_p = 2\,\mathrm{N}$, were used to connect the model to the carriage. Pre-tension is needed to avoid slack due to horizontal motion when testing in waves and current.

Vertical accelerations were measured by accelerometers at eight different positions with an equal interval of 45 degrees. The accelerometers will be refereed from now on by acc fore, acc aft, acc starboard, acc portside, acc 45, acc 135, acc 225 and acc 315, correspond to the position 0, 90, 180, 270, 45, 135, 225 and 315 on the torus.

The wave elevation was measured six different places around the model. Three were placed in front of the model, two on both sides of the model and the last were placed behind the model. A snapshot of the experimental set-up for the model is shown in Figure 4.2.

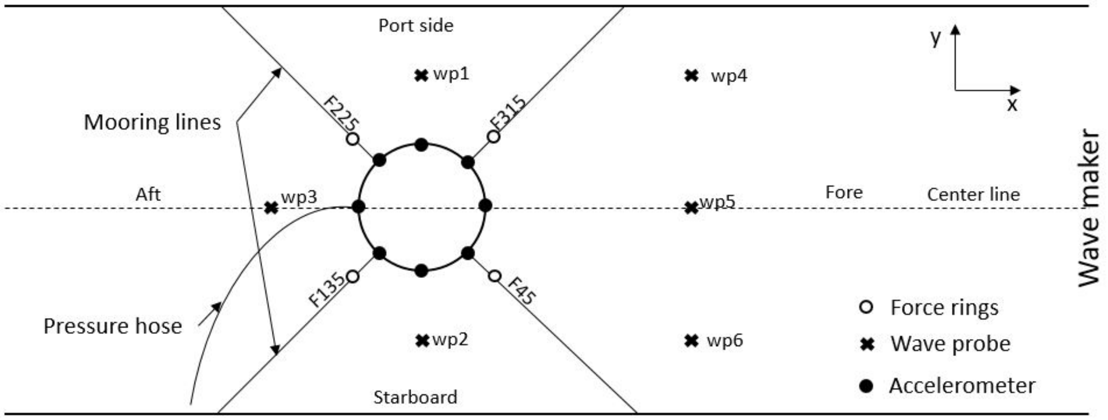

Figure 4.1: Experimental set-up from a top view.

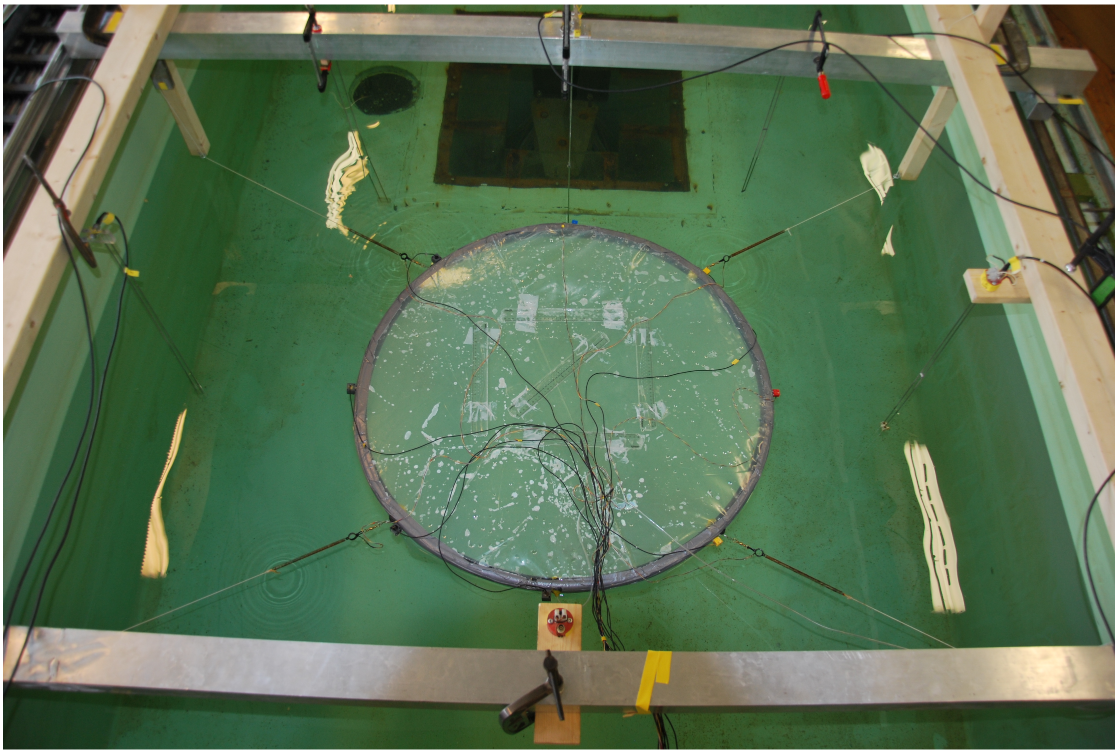

Figure 4.2: Snapshot of the experimental set-up from a top view. In the student model tank at NTNU. The tank is 25 m long, 2.5 m wide and 1.2 m deep. The model was attached with four horizontal mooring lines. The vertical acceleration was measured by accelerometers at eight different positions. The wave elevation was measured six different places around the model.

4.2 Test Conditions

Waves used in the experiment were; incident regular waves with prescribed wave steepness $H/\lambda = 1/50$, $1/40$, $1/30$ and $1/20$ propagating along the x-axis. The wave period $T = 2\pi/\omega$ varied within 4.2-11.4 s with a step of 0.35 s. Regular waves with current equal to 1 m/s. Irregular wave with constant $T_p = 12$ s and H_s varying from 1-8 m with a step of 1 m and irregular waves for the areas given in Table 2.2. All the values are given in full scale and are scaled according to Table 2.3. Table 4.2 shows the test condition for the different models.

	Elastic Model	**Rigid Model**	**Elastic Torus w/membrane**	**Elastic Torus**
Reg wave = 1/30	x	x	x	x
Reg wave = 1/50-1/20	x	-	-	-
Current and wave	x	x	-	-
Irr West-Africa	x	x	-	-
Irr varying H_s	x	x	-	-

Table 4.2: Test matrix for the different models.

4.3 Pressure Measurement

There was no measurement of the actual pressure inside the air cushion during the experiment, and the exact pressure is therefore not known. When the pressure is mention in the result it is referred to the output pressure from the compressor. The pressure was read visual from a gauge meter shown in Figure 4.3. During the test, the pressure was between the value 0.01-0.03 bar. The cushion plenum height can be found for a given pressure by Equation (3.9). Using the pressure values read from the gauge meter, will lead to a cushion plenum height between 0.1-0.3 m. This is not the case since this will mean that the hole model would be out of water. The actual pressure inside the air cushion is therefore expected to be lower than the output pressure.

Figure 4.3: The output pressure from the compressor during the experiment.

4.4 Analysis of the Experimental Results

For the regular wave test the result are taken when steady state is reached. This is done to analyze the results in the frequency domain. In transient conditions the problem must be solved in time (Greco, 2016). Transient effects will exponentially decay with the time (Li, 2017), an example of steady state is shown in Figure 4.4. The data in the steady state region is filtered to remove noise from the measurement and obtain the desired result.

The amplitude of first and second harmonics for the instrumentation are found by a band-pass filtering of the process, the lower and upper cut-off frequencies are $0.95/T$ and $1.05/T$, $1,95/T$ and $2.05/T$. Where T is the wave period for the regular wave. An example of the filtering is shown in appendix C.

The vertical motion is found by integrating the measured accelerations twice in time

$$w(t) = \int_0^t \int_0^{\tilde{t}} \ddot{w}(t')dt'd\tilde{t} \tag{4.1}$$

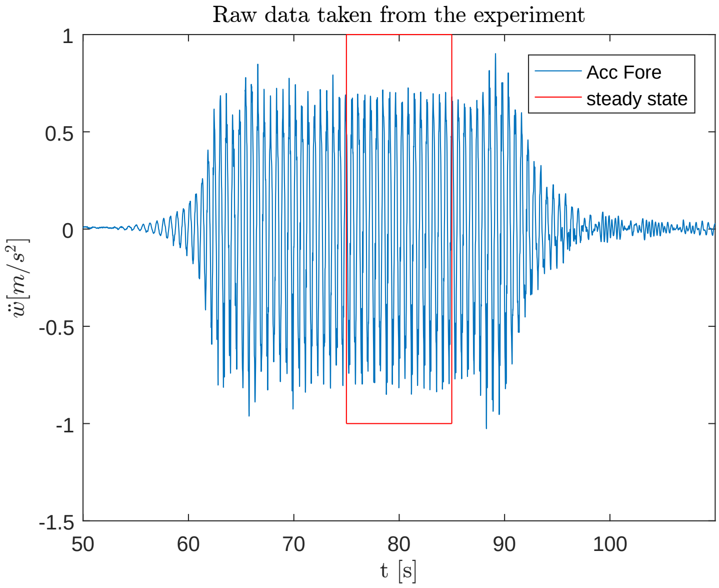

Figure 4.4: Raw data of the vertical acceleration at the front on the elastic model and an example for a steady-state window.

4.4.1 Modal Theory

The coefficient for heave and pitch, a_0 and a_1 are found experimental from a modal analysis of the vertical response. For a linear system, the total periodic response can be determined by superposition of the response from each single component (Larsen & Norges teknisk-naturvitenskapelige universitet Institutt for marin, 2012). This means that the motion can be described by the following equation.

$$w(z,t) = \sum_{n=0}^{N} a_n(t)\Psi_n(z) \tag{4.2}$$

Here $\Psi_n(z)$ is the mode n, a_n the time varying scaling of $\Psi_n(x)$. Using the assumption made in Chapter 3, the mode can be written as $\cos(n\beta)$. The vertical motion around the floater were measured at eight different places, this will lead to the following equation.

$$\begin{aligned} w_1(t) &= \sum_{n=0}^{N} a_n(t)\cos(n\beta_1) \\ &\vdots \\ w_8(t) &= \sum_{n=0}^{N} a_n(t)\cos(n\beta_8) \end{aligned} \tag{4.3}$$

Here w_m is the measured vertical motion given from the experiment, β_m corresponds to the placement of the accelerometers. We are only interested in the first two modes, n = 0 heave, and n = 1 pitch. The following equation system arises

$$\underbrace{\begin{bmatrix} 1 & 1 \\ 1 & \frac{\sqrt{2}}{2} \\ \vdots & \vdots \\ 1 & \frac{\sqrt{2}}{2} \end{bmatrix}}_{\boldsymbol{A}} \underbrace{\begin{bmatrix} a_0(t) \\ a_1(t) \end{bmatrix}}_{\boldsymbol{a}} = \underbrace{\begin{bmatrix} w_1(t) \\ w_2(t) \\ \vdots \\ w_8(t) \end{bmatrix}}_{\boldsymbol{b}} \tag{4.4}$$

The solution to Equation (4.4) can be found by

$$\boldsymbol{a}(t) = [(\boldsymbol{A}^T\boldsymbol{A})^{-1}\boldsymbol{A}^T]\boldsymbol{b}(t) \tag{4.5}$$

4.4.2 Irregular Waves

The spectral analysis is done by use of Fast Fourier Transform. From the input wave spectrum and measured response spectrum, the response amplitude operator $|H(\omega)|$, can be determined by (Steen, 2014)

$$|H(\omega)|^2 = \frac{S_{yy}(\omega)}{S_{xx}(\omega)} \tag{4.6}$$

Here $S_{xx}(\omega)$ is the input spectrum and $S_{yy}(\omega)$ is the measured response spectrum. Using Equation (4.6) no phase information between the input and response is obtained.

Chapter 5

Results and Discussion

The regular wave test for the elastic model were repeated eight times. For the rigid model and the elastic torus, the test was only repeated three times due to limiting time. Raw data for the elastic model in regular waves are shown in appendix B. The result for the elastic torus covered with membrane are shown in appendix A.

5.1 Visual Observation from the Experiment

Together with the master thesis report a movie is attached. The movie contains;

- Comparison between the elastic and rigid model in current at 1 m/s and in incident regular waves with steepness 1/50. Wave period 4.20 s, 5.95 s, 7.70 s and 9.45 s.
- A front view of the elastic model in regular waves with steepness 1/20 and wave period 10.00 s.
- A rear view of the elastic model in regular waves with steepness 1/20 and wave period 12.10 s.
- A front view comparison between the elastic and rigid model in regular waves with steepness 1/20 and wave period 12.10 s.

- A rear view of the elastic model in irregular sea with $H_s = 5.0\,\mathrm{m}$ and $T_p = 12.0\,\mathrm{s}$

The global behavior for the rigid and elastic model is different. The elastic model tends to follow the waves, while the rigid model moves as a single unit. Non-linear phenomena such as out of water and over-topping of the waves is seen in the movie in regular waves with steepness = 1/20 and period 12.10 s. For both models, the phenomena lead to flooding of the model. This problem needs to be addressed in the design processes.

The flooding takes longer time for the rigid model, this can be due to the pressure underneath the membrane. For the elastic model, it is seen that the pressure is exposing the skirt more than for the rigid model. The skirt exposure may be the reason why the flooding happens faster for the elastic model.

Over-topping of the waves is also happening in irregular waves for $H_s = 5\,\mathrm{m}$ and $T_p = 12\,\mathrm{s}$. In this case flooding of the model didn't occurred since the elastic model was able to drain of the water with the help of the overpressure.

Figure 5.1 and 5.2 shows that the applied overpressure has a significant influence on the static stability of the solar island in calm water. For zero output pressure for the compressor (left picture) the model is symmetrical in the water line. The pressure causes the model to be lifted and the skirt gets exposed. The lifting is not happening symmetrical around the floater. When the output pressure is 0.1 bar almost the entire skirt is exposed. Figure 5.1 and 5.2 shows that the influence of the pressure for the rigid and elastic model is quite different, the elastic model is more locally deformed. Without the pressure, the membrane for the elastic model is not strong enough to carry the weight of the PV panels, and in waves the membrane will stick to the waves.

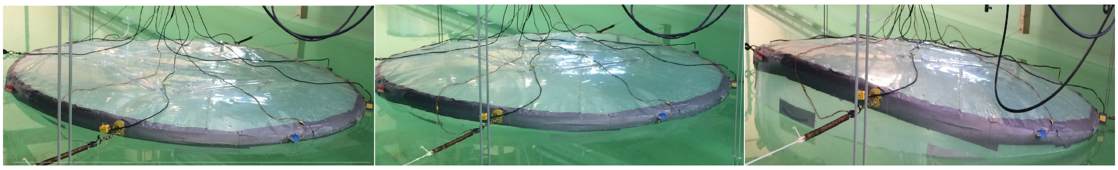

Figure 5.1: Picture of the elastic model in calm water with different overpressure. From left P = 0 bar, P = 0.01 bar and P = 0.1 bar. The value of the pressure is taken from the output pressure to the compressor.

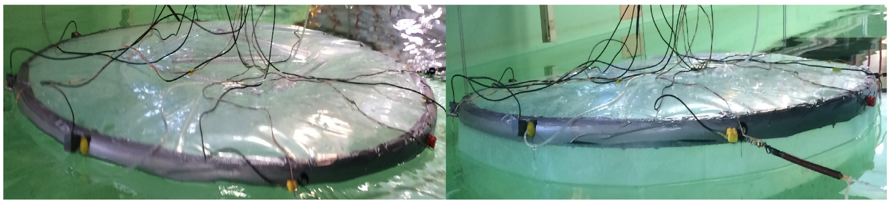

Figure 5.2: Picture of the rigid model in calm water with different overpressure. From left P 0 bar and P = 0.1 bar. The value of the pressure is taken from the output pressure to the compressor.

Figure 5.3 shows snapshots of the elastic model in regular waves with steepness = 1/20 and wave period 10.0 s, at a front view. The figure shows that almost the entire skirt is exposed to air. Out of water can be critical as it can lead to failure. It can also lead to large local forces and should be considered when fatigue life of the solar island is designed.

Figure 5.4 shows snapshot of the elastic model in regular waves with steepness = 1/20 and wave period T=12.1 s, at a rear view. In this wave condition, the aft of the torus gets under water and the water starts to flood the membrane. This is critical since this process will lead to that the island will be completely flooded. Figure 5.5 shows the rear view of the floater after the island has been flooded.

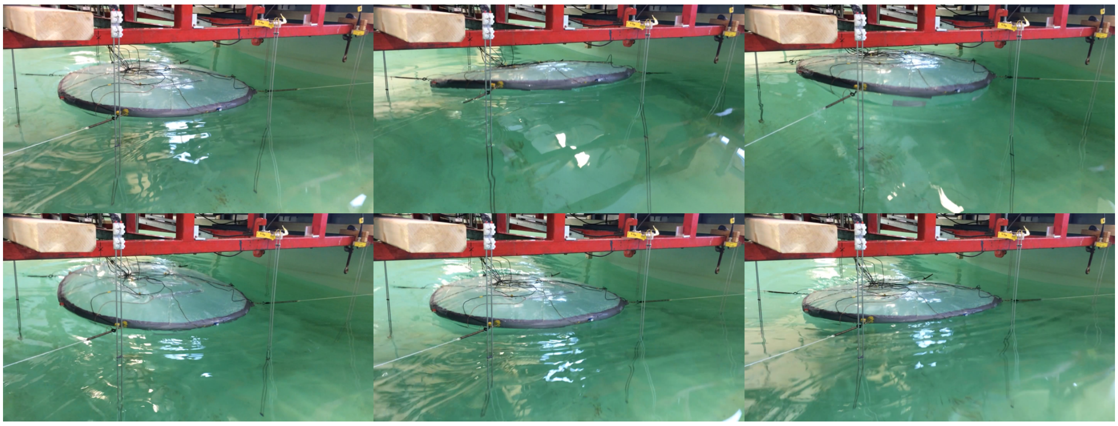

Figure 5.3: Snapshot from the film of the elastic model in regular waves with steepness = 1/20 and a wave period at T = 10.0 s, front view.

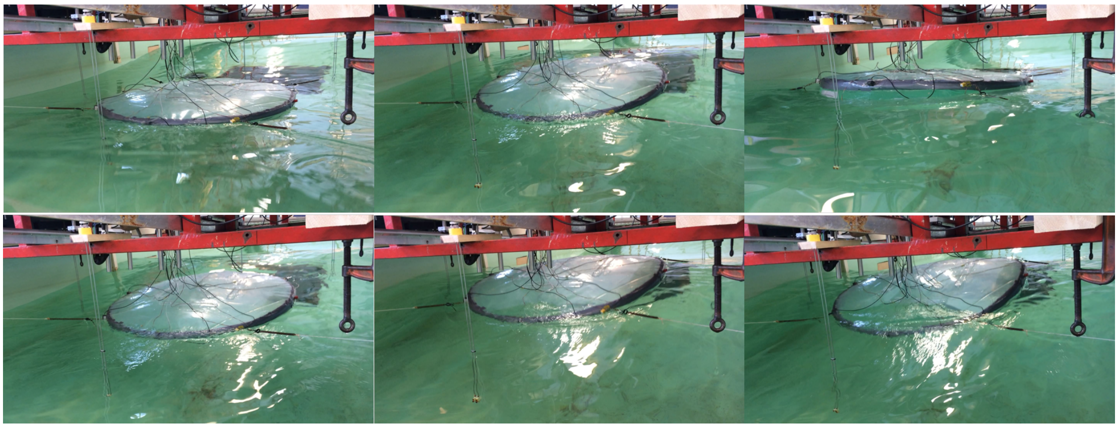

Figure 5.4: Snapshot from the film of the elastic model in regular waves with steepness = 1/20 and a wave period at T = 12.1 s, rear view.

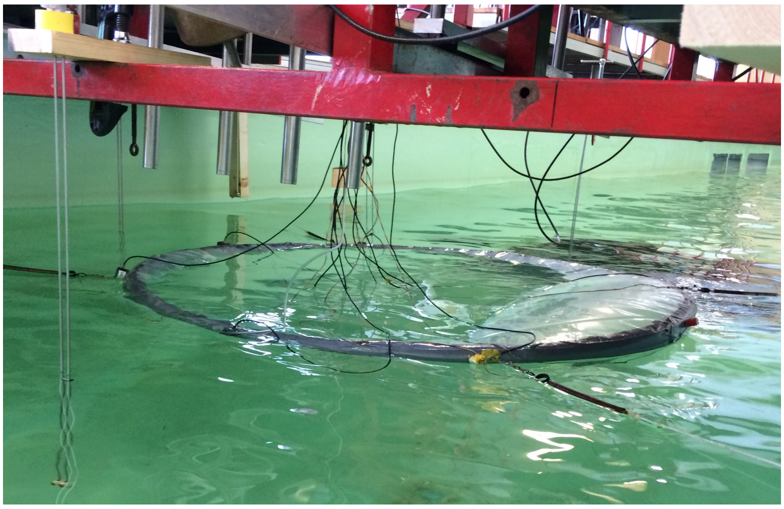

Figure 5.5: Rear view of the elastic model that has been flooded. In regular waves with steepness = 1/20 and a wave period at T = 12.1 s.

5.2 Response Amplitude Operator in Heave

Figure 5.6 shows the experimental results in heave for regular waves with steepness 1/30, compared with the numerical model. The experimental results are from the elastic model with pressure, the rigid model with and without pressure and for the elastic torus. The vertical motion is then divided by the wave amplitude measured by the wave probes. The numerical models are calculated by use of Equation (3.58) and (3.59). In the figure, the experimental result is presented as error bares, where the height of the bars is two times the estimated standard deviation.

Figure 5.6 shows satisfactory agreement between the experimental and numerical results. The results show that the membrane is influencing the vertical response. For low wave frequencies, the heave response is larger with the membrane, for higher frequencies the response is considerably reduced. This is the same result found in Pinkster and Fauzi (1997).

There are some differences in the vertical response for the models. The difference can be due to bending stiffness, but since the numerical model don't account for

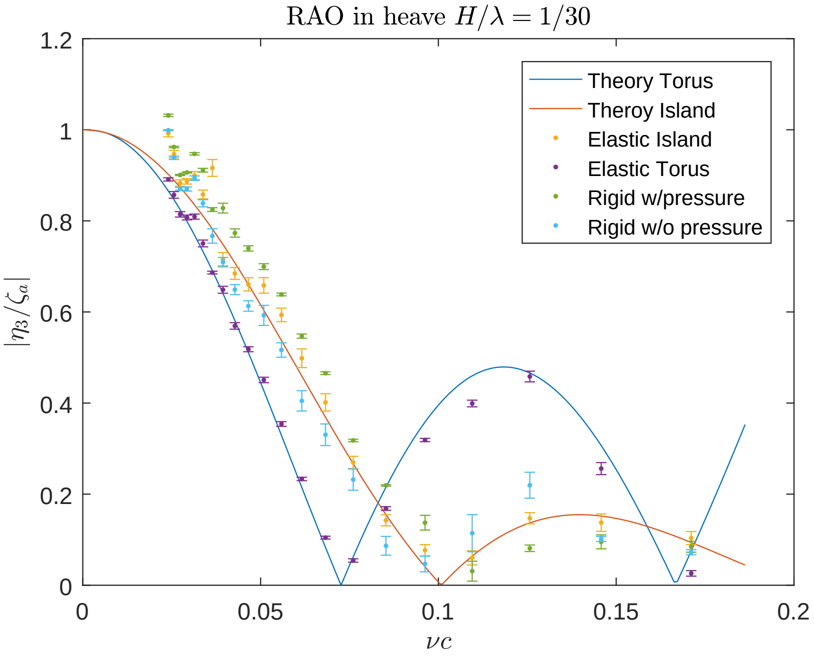

Figure 5.6: RAO in heave for the experimental result, for the rigid model with and without overpressure, the elastic model and the elastic torus. The height of the experimental error bars is two times the estimated standard deviation. Theory for the torus is from Equation (3.59). The theory for the solar island is from Equation (3.58).

the stiffness. It is more likely that the difference can be due to pressure underneath the air cushion. Like a spring where the force is $F = kx$, the pressure will lead to a stiffness inside the air cushion. Larger pressure will lead to a higher stiffness i.e. more of the wave gets transmitted to the membrane.

In Figure 5.6 the pressure used in the numerical calculations is 20 Pa, this value were taken since it was the best fit. Figure 5.7 shows a sensitive study on the pressure used in the numerical model for the vertical response. The pressure is varying from 0 Pa-25 000 Pa and $p \to \infty$. 25 000 Pa = 0.025 bar which is the middle value for the output pressure from the compressor. The numerical results show that increasing the pressure will lead to a reduction in the response for high wave frequencies. For low wave frequencies, the heave response gets larger. The difference in the result for $p = 148$ Pa and $p \to \infty$ is small, due to the terms involving the pressure becomes large compared with the other terms.

The rigid model with pressure is closer to the numerical result with pressure equal 148 Pa than 20 Pa. This can be an indication that the pressure for the rigid model was higher compared with the pressure for the elastic model. The displaced water inside the air cushion can be found by Equation (3.9). For pressure 148 Pa the displaced water is 0.015 m. The displacement is close to the cross-sectional diameter of the model and can be feasible.

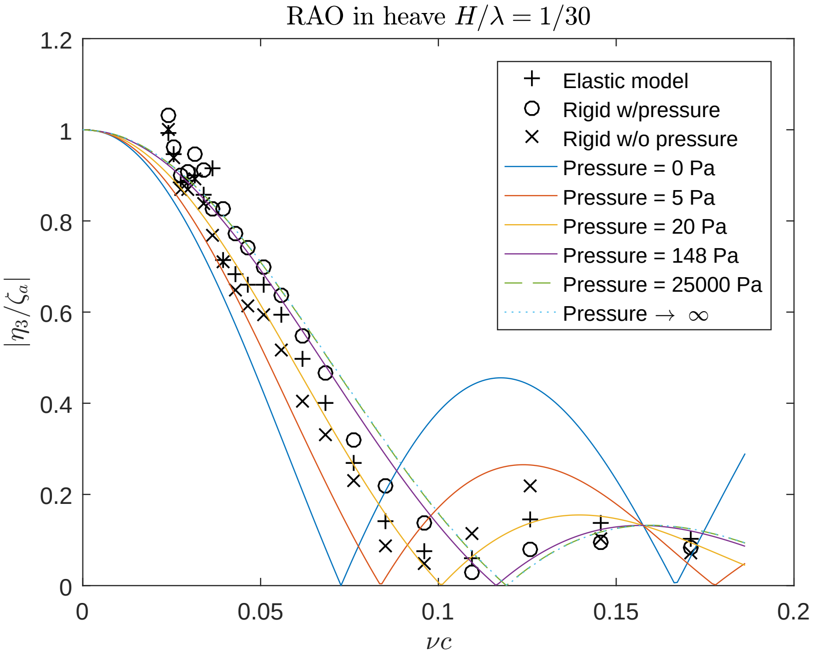

Figure 5.7: A sensitive study of the influence of the pressure used in the numerical model compared with the experimental results for the rigid model with and without overpressure and the elastic model.

5.3 Response Amplitude Operator in Pitch

Figure 5.8 shows the experimental result for the elastic torus in regular waves with steepness 1/30, compared with the numerical model for the torus. The numerical model are calculated by use of Equation (3.75) with two different stiffness, $EI = 0.46\,\mathrm{Nm}^2$ elastic and $EI = 23.74\,\mathrm{Nm}^2$ rigid. In the figure, the result is presented as error bars, where the height of the bars is two times the estimated standard deviation.

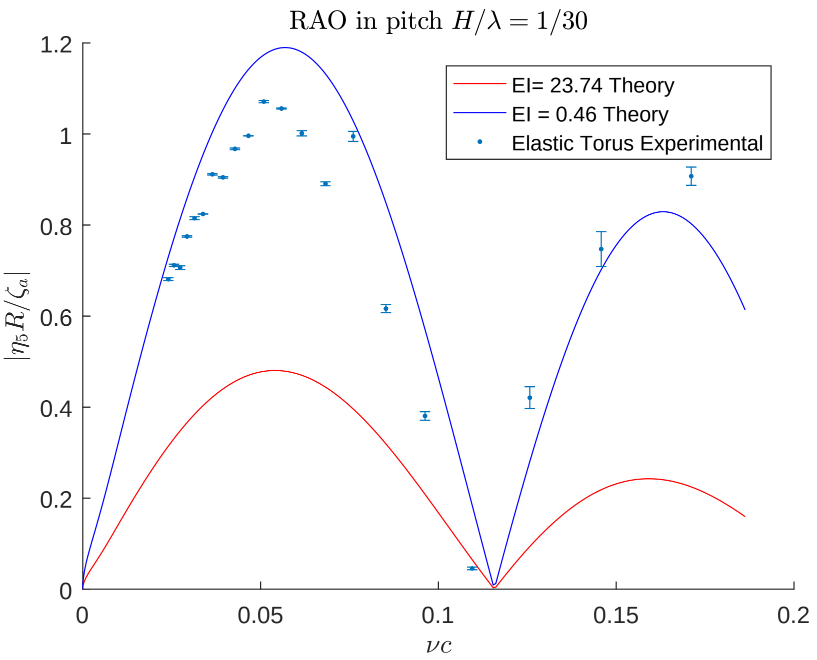

Figure 5.8: RAO in pitch for the experimental result for the elastic torus. The result is compared against Equation (3.75). The equation is calculated with a bending stiffness, $EI = 0.46\,\mathrm{Nm}^2$ elastic, and $EI = 23.74\,\mathrm{Nm}^2$ rigid. The height of the experimental error bars is two times the estimated standard deviation.

Figure 5.8 shows that the experimental and numerical results has the same trend. The experimental results are found to be a little lower than the numerical result which indicate that the elastic torus has higher stiffness than used in the numerical model. For the highest wave frequency, the numerical model is lower than the experimental result.

Figure 5.9 shows the experimental results in pitch for regular waves with steepness 1/30, compared with the numerical model for the torus (solid lines) and the numerical model for the island (dotted lines). The experimental results are from the elastic model, the rigid model with and without pressure and the elastic torus. The numerical models are calculated by use of Equation (3.75) and (3.77) with pressure equal to 5 Pa.

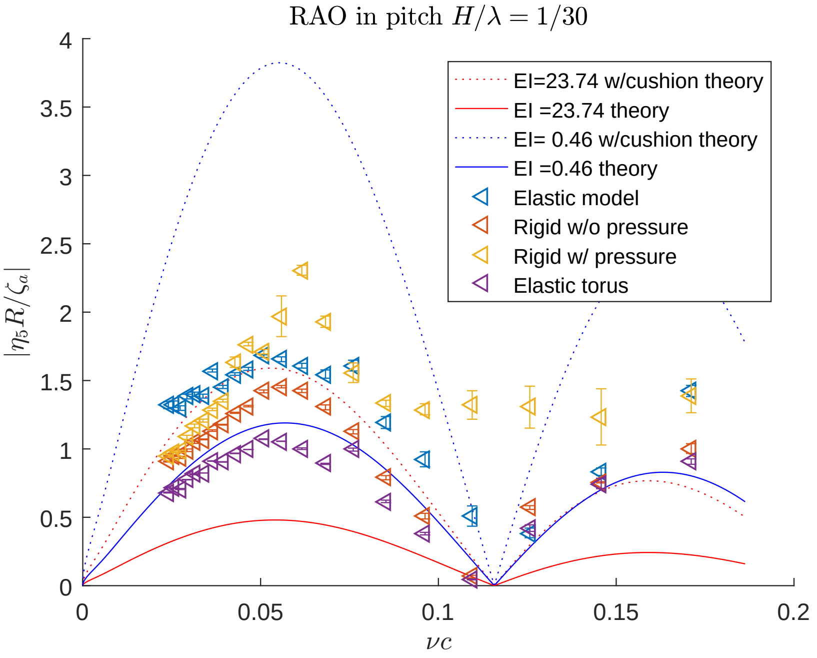

Figure 5.9: RAO in pitch for the experimental result, for the rigid model with and without overpressure, the flexible model and only floater. The result is compared against the theory for the torus(solid), Equation (3.75) and the theory including the effect of the air cushion(dotted line), Equation (3.77). The equation is calculated with a bending stiffness, $EI = 0.46\,\mathrm{Nm}^2$ elastic, and $EI = 23.74\,\mathrm{Nm}^2$ rigid. The height of the experimental error bars is two times the estimated standard deviation.

The experimental result in Figure 5.9 shows that the pitch motion for the elastic and rigid model is similar. While the numerical result shows that there is a difference between the rigid and elastic model. The experimental result for the rigid model without pressure are in agreement with the numerical result. The numerical and experimental result shows that the membrane will increase the pitch motion. The result for the rigid model with pressure does not have the same trend as the two other results. This can be due to the pressure underneath the air cushion.

5.4 Acceleration from the Regular Wave Test

In the figures that follows the mean values of the steady state amplitude of the accelerations are plotted against the non-dimensional wave number νc where $\nu = \frac{\omega^2}{g}$ and c is the cross-sectional radius. The harmonic acceleration is then made non-dimensional by $R/\zeta_a g$, this is done in order to compare the magnitudes of the harmonic terms.

5.4.1 First Harmonic Acceleration

Figure 5.10 and 5.11 shows the first harmonic of the vertical acceleration for the elastic model. Figure 5.13 and 5.12 shows the first harmonic acceleration for the rigid model without overpressure. Figure 5.14 and 5.15 shows the first harmonic acceleration for the rigid model with pressure. Figure 5.16 shows the first harmonic acceleration for the elastic torus.

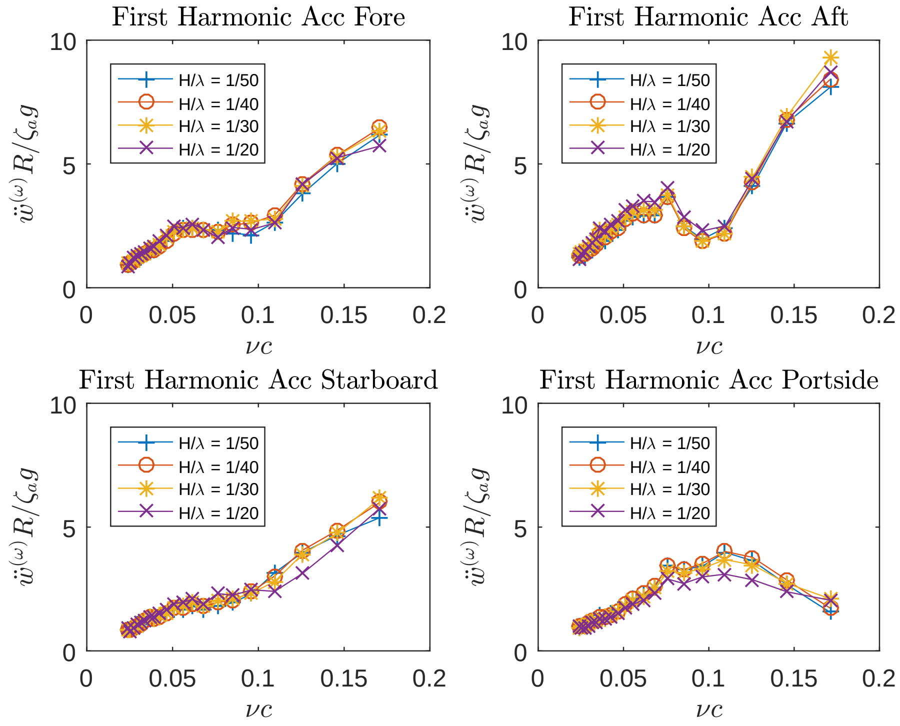

Figure 5.10: The elastic model non-dimensional amplitudes of first harmonic vertical acceleration versus the non-dimensional wave number νc for regular waves with steepness 1/50, 1/40, 1/30 and 1/20. At front, left, right and aft position on the torus.

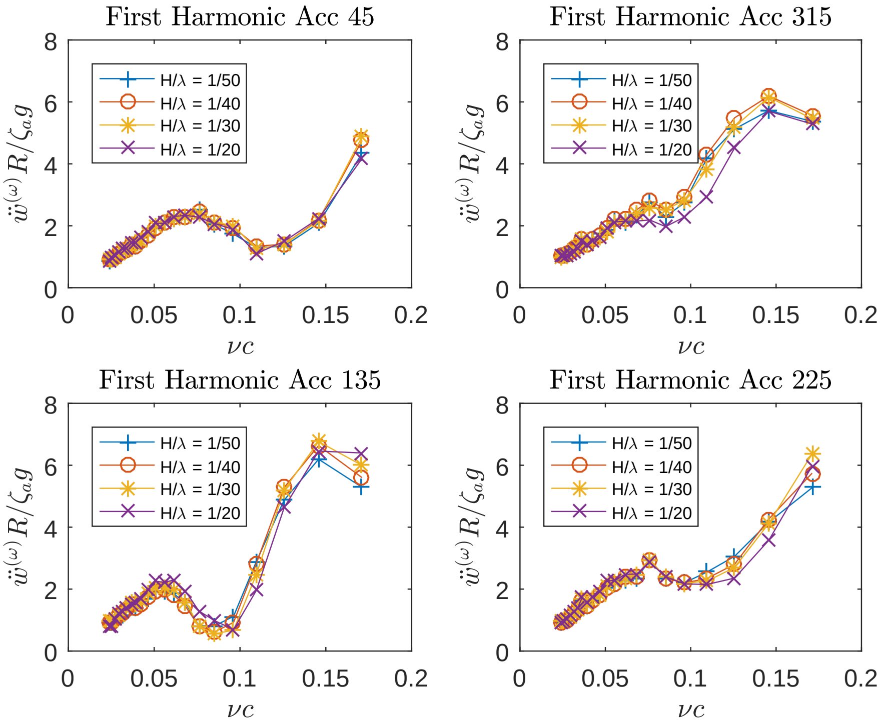

Figure 5.11: The elastic model non-dimensional amplitudes of first harmonic vertical acceleration versus non-dimensional wave number νc for regular waves with steepness 1/50, 1/40, 1/30 and 1/20. At the position 45 ,135, 225 and 315.

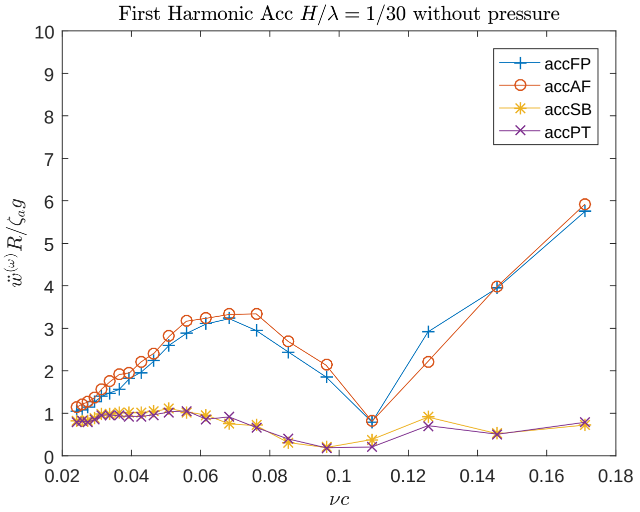

Figure 5.12: The rigid model without pressure, non-dimensional amplitudes of first harmonic vertical acceleration versus non-dimensional wave number νc for regular waves with steepness 1/30. At front, left, right and aft position on the torus.

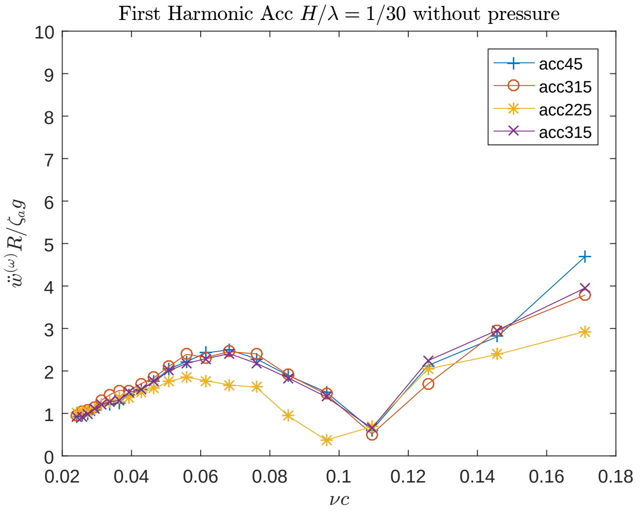

Figure 5.13: The rigid model without pressure, non-dimensional amplitudes of first harmonic vertical acceleration versus non-dimensional wave number νc for regular waves with steepness 1/30. At the position 45, 135, 225 and 315.

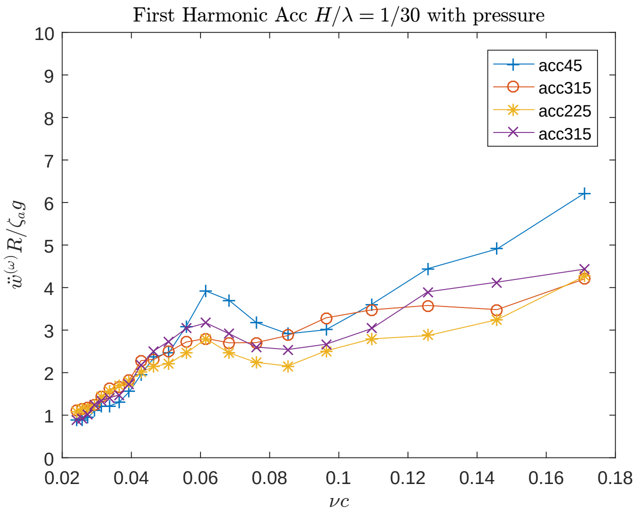

Figure 5.14: The rigid model with pressure, non-dimensional amplitudes of first harmonic vertical acceleration versus non-dimensional wave number νc for regular waves with steepness 1/30. At the position front, aft, right and left position on the torus.

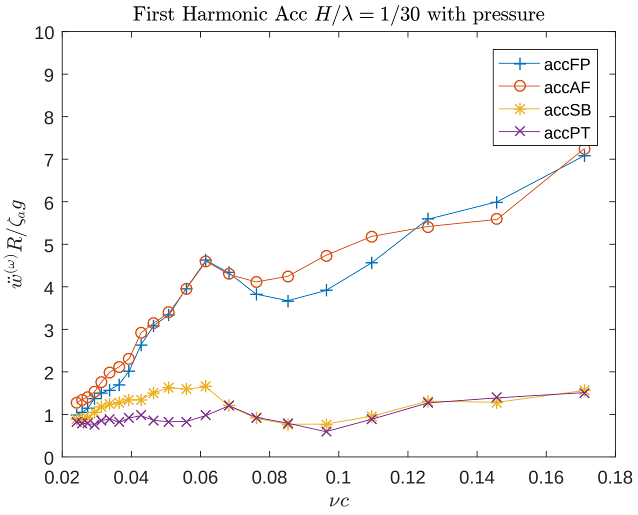

Figure 5.15: The rigid model with pressure, non-dimensional amplitudes of first harmonic vertical acceleration versus non-dimensional wave number νc for regular waves with steepness 1/30. At the position 45, 135, 225 and 315.

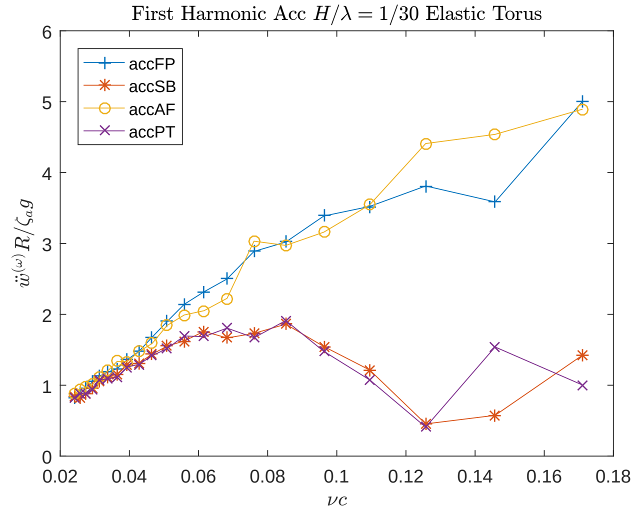

Figure 5.16: The elastic torus, non-dimensional amplitudes of first harmonic vertical acceleration versus non-dimensional wave number νc for wave steepnesses 1/30. At front ,left, right and aft position on the torus.

The amplitude of first harmonic vertical acceleration for the elastic torus, Figure 5.16, are in good agreement with the experimental results in Li et al. (2014). For the lowest wave frequencies, the non-dimensional amplitude of the acceleration is close to one for all accelerometers i.e. the model is following the wave. For higher wave frequencies, the non-dimensional amplitude of the acceleration becomes larger front and aft at the model. The results for the elastic torus shows symmetrical behavior for the accelerations.

By comparing the experimental result for the vertical acceleration for the elastic model and elastic torus, Figure 5.10 and 5.16. The experimental results show that the membrane will increase the value of the non-dimensional amplitudes. The acceleration is still largest front and aft at the model.

Figure 5.10 and 5.11 shows that the acceleration are linear dependent on the incoming regular waves. The figure shows that the accelerations are not symmetrical around the torus as found from the other experimental results. This is probably due to the applied overpressure that makes the model unsymmetrical in the water line, as illustrated in figure 5.1, and the fact that the elastic model can follow the incoming waves.

Figure 5.13, 5.14, 5.12 and 5.15 shows the amplitude of the vertical acceleration for the rigid model with and without pressure. The experimental results show that the vertical acceleration is larger compared with the elastic torus. Comparison of the experimental results shows that the amplitude of accelerations is larger for the rigid model with pressure than without. The result indicates that the pressure will increase the vertical acceleration. The amplitude for the rigid model with pressure is higher than the amplitude for the elastic model, except for the highest wave frequency. This can also be an indication that the pressure under the air cushion for the rigid model was higher compared with the elastic model.

5.4.2 Second Harmonic Acceleration

Figure 5.17 and 5.18 shows the second harmonic of the vertical acceleration for the elastic model. Figure 5.19 and 5.20 shows the second harmonic of vertical acceleration for the rigid model, with and without pressure.

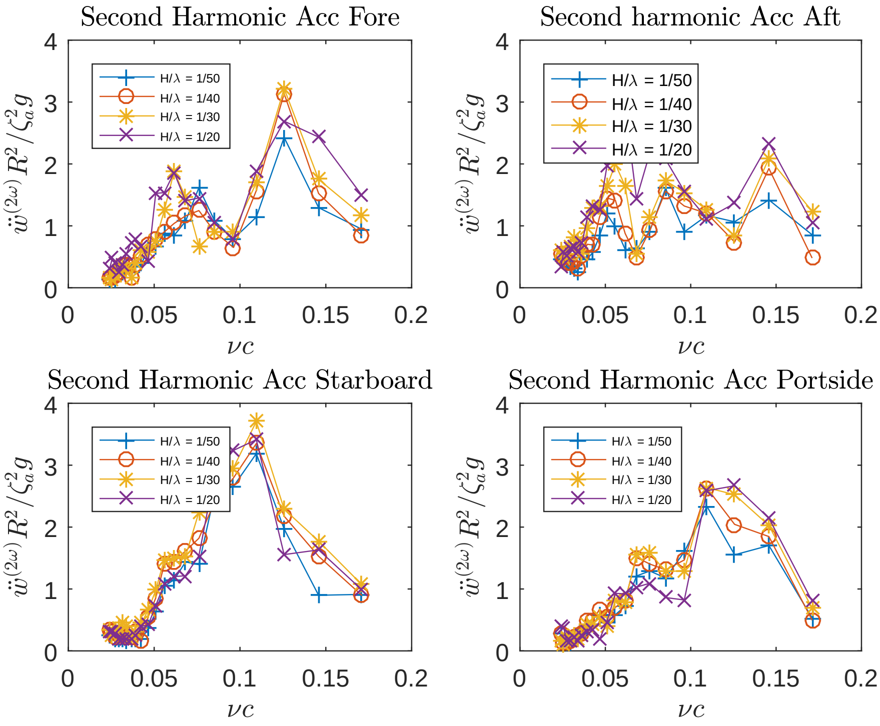

Figure 5.17: The elastic model non-dimensional amplitudes of second harmonic vertical acceleration versus non-dimensional wave number νc for regular waves with steepnesses 1/50, 1/40, 1/30 and 1/20. At front ,aft, right and left position on the torus.

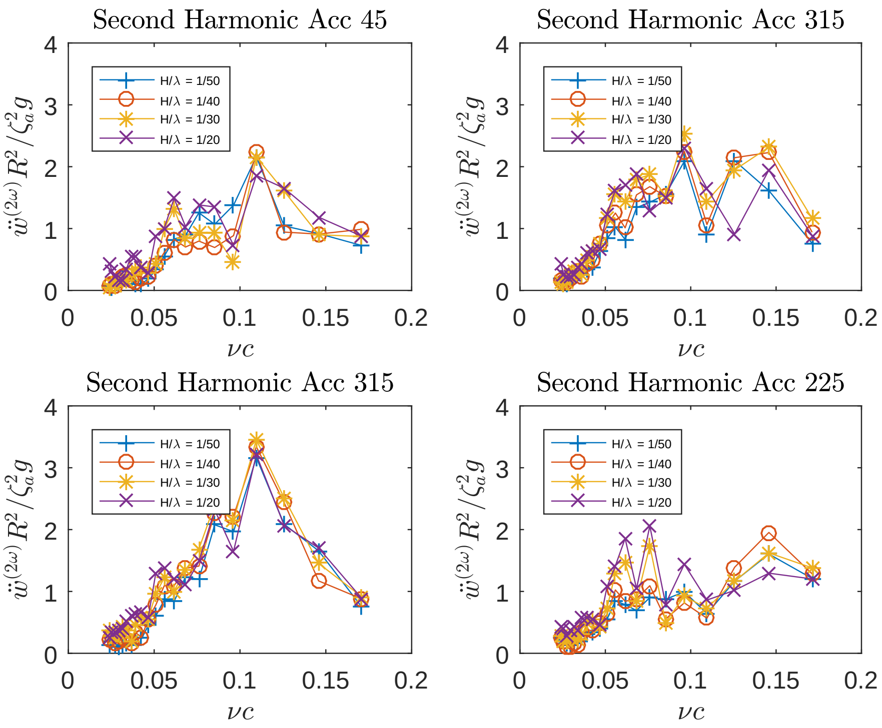

Figure 5.18: The elastic model non-dimensional amplitudes of second harmonic vertical acceleration versus non-dimensional wave number νc for regular waves with steepnesses 1/50, 1/40, 1/30 and 1/20. At the position 45 ,135, 225 and 315.

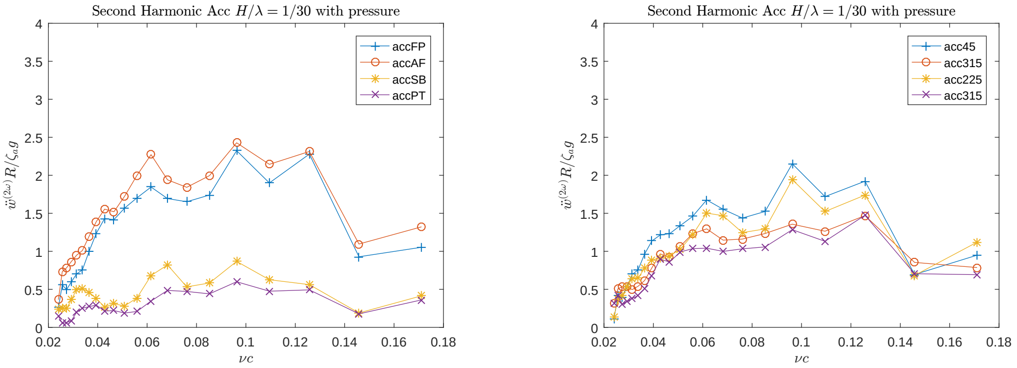

(a) Position front, left, right and aft.

(b) Position 45, 135, 225 and 315.

Figure 5.19: The rigid model with pressure, non-dimensional amplitudes of second harmonic vertical acceleration versus non-dimensional wave number νc for regular waves with steepness 1/30.

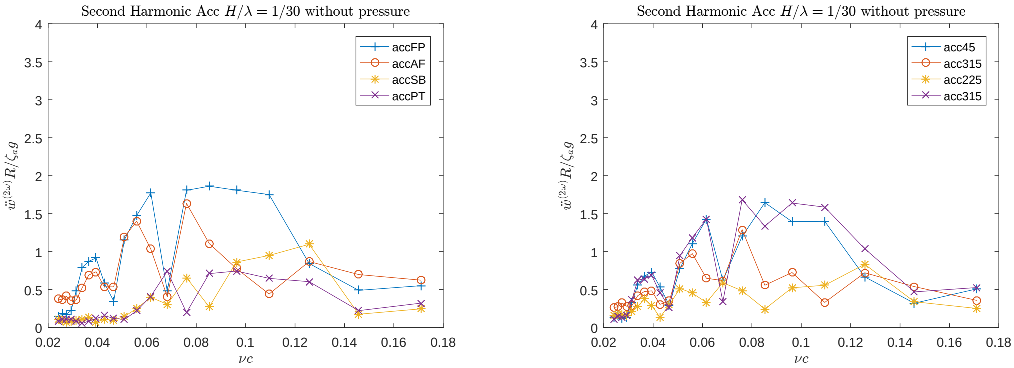

(a) Position front, left, right and aft.

(b) Position 45, 135, 225 and 315.

Figure 5.20: The rigid model without pressure, non-dimensional amplitudes of second harmonic vertical acceleration versus non-dimensional wave number νc for regular waves with steepness 1/30.

From the figures 5.20, 5.19, 5.18 and 5.17 it can be seen that the second harmonic acceleration matter. The accelerations are higher for the elastic model compared with the rigid model with and without pressure. Higher order harmonics of the wave loads can be significant when resonance oscillations are excited and should be taken into account when fatigue life of the solar island is designed (Li, 2017).

5.5 Wave Probes

Figure 5.21 show the experimental results for the six wave probes used in the experiment, the result are compared with the theoretical wave amplitude. The wave amplitudes are calculated as the sum of first and second harmonic. The results are plotted against the non-dimensional wave number.

Figure 5.21 is showing reasonable agreement between the theory and measured wave amplitudes. The figure shows that the wave generation of the structure is small, since the measured wave elevation around the model is the same. This is as expected since the cross-sectional is small compared to the incoming waves $\lambda/D > 5$. Therefore, the waves generated by the wave-body interaction are small.

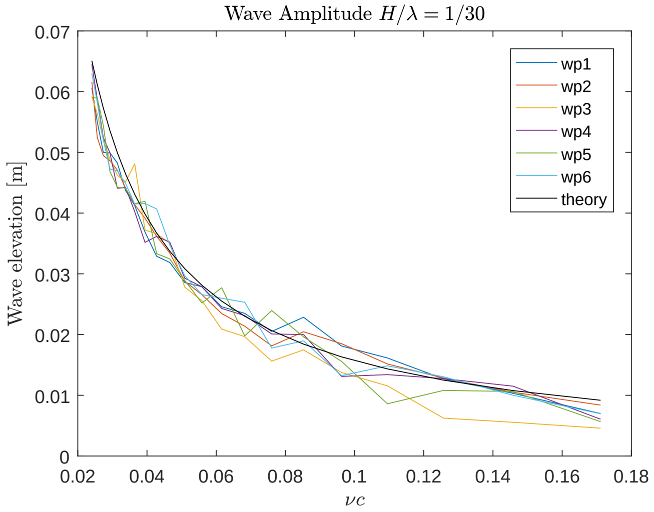

Figure 5.21: Experimental result for the wave probes for the combined first and second harmonic amplitude of the wave elevation for regular waves with steepness 1/30. The result are plotted against the theoretical values for the wave amplitude.

Figure 5.22 compares the first and second harmonic compared to the theory described in Chapter 2. The figure is showing reasonable agreement between theory and experimental result. In the second harmonic amplitude of the wave elevation parasitic waves can been seen. These are not wanted and can pollute the result.

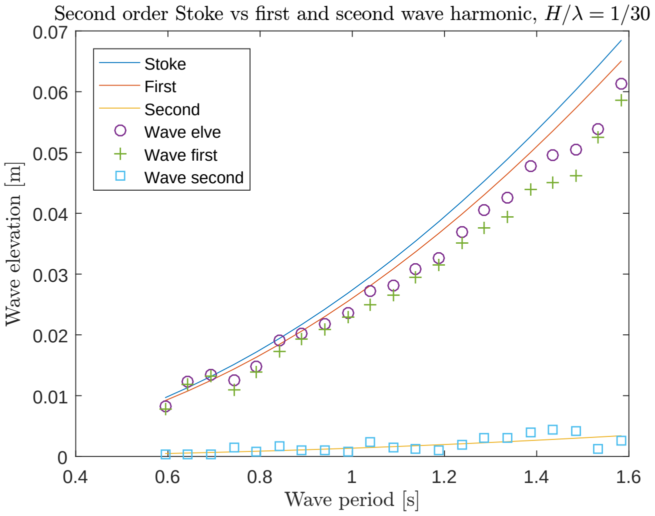

Figure 5.22: First and second harmonic amplitude of the wave elevation fro regular waves with steepness = 1/30. The experimental results are plotted against the theoretical values calculated from Equation (2.1) and (2.3).

5.6 Mooring Force from the Regular Wave Test

The mooring force were measured at four different location on the torus, 45(front), 135(aft), 225(aft) and 315(front). The value of the force are plotted against the non-dimensional wave number νc. Figure 5.23 shows the amplitude of the force for the elastic model. Figure 5.25 shows the amplitude of the force for the rigid model without pressure and Figure 5.24 for the rigid model with pressure. Figure 5.26 shows the amplitude of the force for the elastic torus and Figure 5.27 shows the amplitude of the force for the elastic torus covered with a membrane.

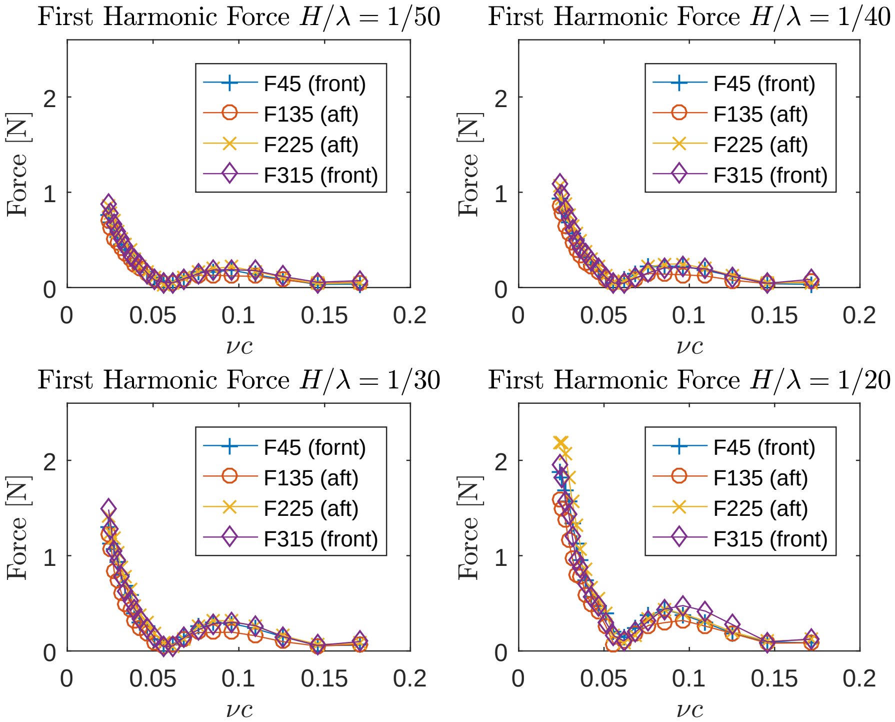

Figure 5.23: Amplitude of the force for the elastic model in the four moorings obtain from the experiment for regular waves with different wave steepness.

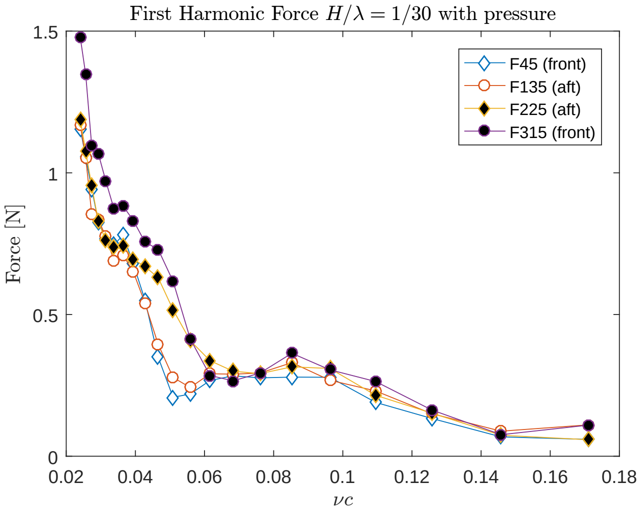

Figure 5.24: Amplitude of the force for the rigid model with pressure in the four mooring lines in regular waves with steepness 1/30.

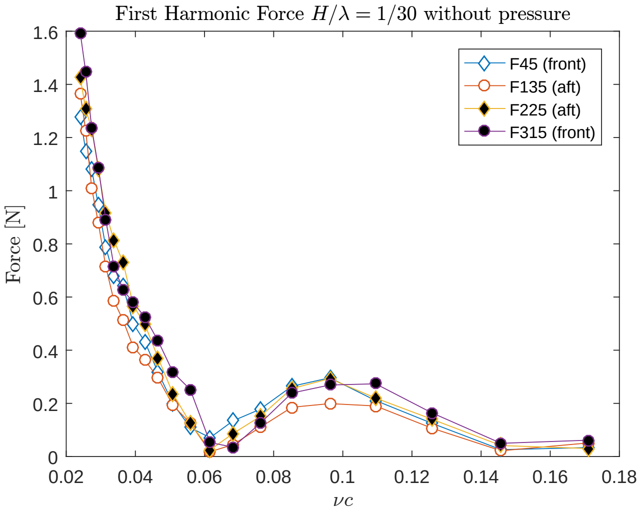

Figure 5.25: Amplitude of the force for the rigid model without pressure in the four mooring lines in regular waves with steepness 1/30.

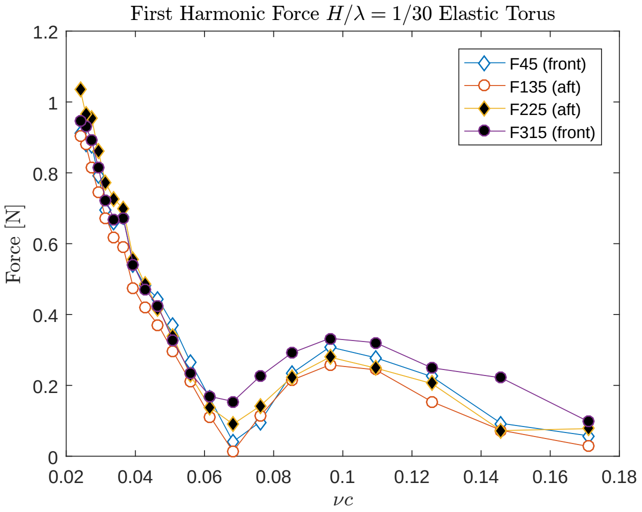

Figure 5.26: Amplitude of the force for the elastic torus in the four mooring lines in regular waves with steepness 1/30.

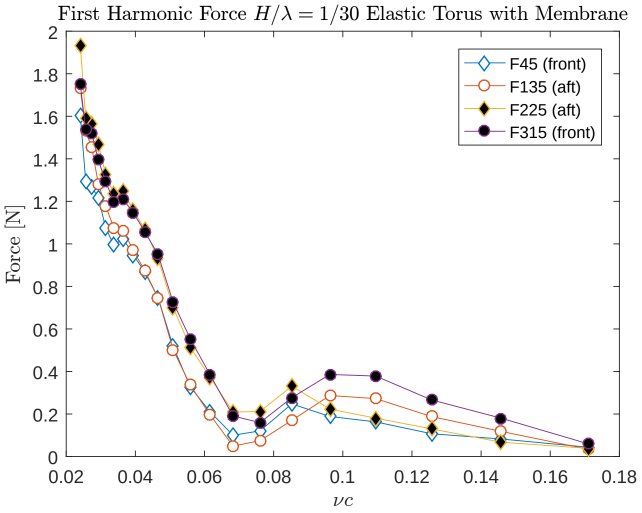

Figure 5.27: Amplitude of the force for the elastic torus with membrane in the four mooring lines in regular waves with steepness 1/30.

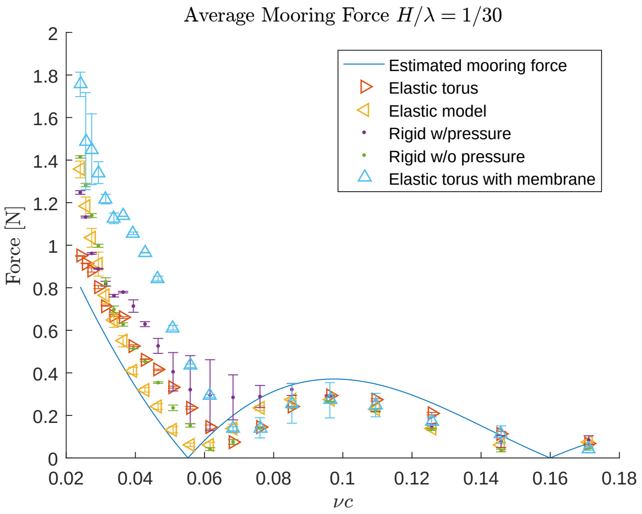

Figure 5.28: The average amplitude of the force from the four mooring lines, for the rigid model with and without overpressure, the elastic model, the elastic torus and the elastic torus covered with membrane. For regular waves with steepness 1/30. The experimental results are plotted against the estimated force in the mooring lines. The height of the experimental error bars is two times the estimated standard deviation.

Figure 5.23 shows that the amplitude of the mooring force for the elastic model is increasing with the wave steepness. The experimental result for the mooring force for the rigid model without pressure and the elastic model, Figure 5.25 and 5.23, are very similar. Both result show that the amplitude of the force is close to zero for the non-dimensional wave number $\nu c = 0.06$ and $\nu c = 0.15$, which indicates that there is a cancellation of the vertical motion around these wave frequencies.

The experimental result for the rigid model with pressure, Figure 5.24, shows that the amplitude of the force is not zero for the non-dimensional wave number $\nu c = 0.06$. The result can be explained by the pressure inside the torus. The influence is shown in Figure 5.2 and will have a larger influence on the horizontal result than the vertical, since the wave force on the skirt is different than for the torus.

Figure 5.28 is showing the average mooring force for the different test and compared with the estimated mooring force. In the figure, the result is presented as error bares, where the height of the bars is two times the estimated standard deviation.

The experimental results show that the presence of the membrane leads to a higher average force in the mooring line compared with the elastic torus. By comparing the models with the torus covered with a membrane, it is shown that the skirt will give a lower average force in the mooring lines for the lowest wave frequencies. This is because the presence of the skirt will increase the added mass in surge. The addition in added mass will give lower horizontal movement hence the mooring force becomes less.

The estimated mooring force are calculated by Equation (3.87). When calculating surge motion only the torus was considered, the calculation is also neglecting any coupling between horizontal and vertical motion. The values of the estimated mooring force are comparable with the experimental result for the elastic floater. The estimated mooring force is higher for high wave frequencies, and lower for lower wave frequencies. The experimental result for the elastic torus indicates that the cancellation is around $\nu c = 0.067$ and $\nu c = 0.16$ while the estimated predicts $\nu c = 0.058$ and $\nu c = 0.16$. A reason for the difference can be due to the neglecting of any coupling between the motions.

5.6.1 Dynamic Load Factor

The dynamic load factor (DLF) can be used to determine if the system response is stiffness or inertia dominated. Figure 5.29 shows the DLF plotted against the frequency ratio $\beta = \omega/\omega_0$. The DLF is not for the system as this would require knowledge of the damping, but it is used as an illustration for the different load regions. The dots in the figure are the frequency ratio between the incoming waves in the experiment and the natural frequency of the elastic torus with mooring. The natural frequencies are found by use of Equation (3.88), and it is equal to $\omega_0 = 3.27\,\text{rad/s}$. A more accurate way to find the natural frequency is through a decay test. A decay test will give important information about natural frequencies, added mass and damping of the system (Steen, 2014). No experimental decay test was done in this study.

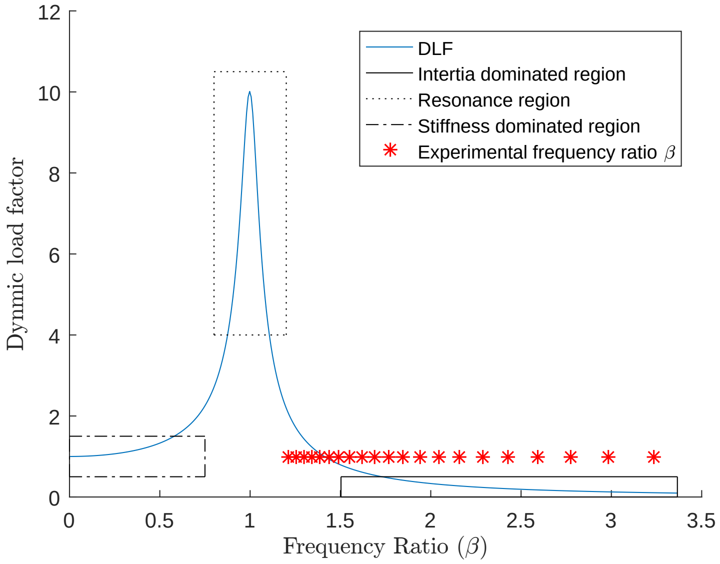

Figure 5.29: Dynamical load factor plotted against the frequency ratio β. The points are the experimental frequency ratio between the incoming waves and the natural period for the surge motion for the elastic torus.

Figure 5.29 shows that the response given the load condition is inertia dominated. This means that the inertia forces balance the external forces. The restoring force is in fact increasing the response. Therefore, the moored platform has a larger dynamic motion in waves than what the same platform would have had if it was floating freely without a mooring system (Larsen & Norges teknisk-naturvitenskapelige universitet Institutt for marin, 2012). For the lowest wave frequencies, the response is in the resonance region.

The natural frequency for the island will be lower since the skirt will increase the added mass. A lower natural frequency will give higher β values meaning that the islands also will be in the inertia dominated region.

5.7 Waves and Current

Figure 5.30 show the raw data from the experiment in regular waves with current, taken from the force ring F45 (front) of the rigid model. Figure 5.31 is comparing the first harmonic vertical acceleration aft for the elastic and rigid model in regular waves with steepness $1/30$ and current $1\,\mathrm{m/s}$. Figure 5.32 is comparing the first harmonic vertical acceleration at the front for the elastic and rigid model in wave steepens $1/30$ and current $1\,\mathrm{m/s}$. Figure 5.33 is comparing the force in the four mooring lines, in the same conditions. The non-dimensional wave number is calculated form the encounter frequency to the model. The acceleration front and aft are taken since they were the highest in the regular wave test.

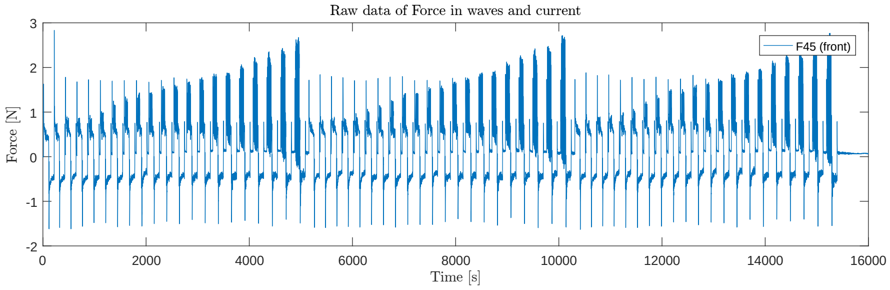

Figure 5.30: Raw data of the mooring force measured at F45(front) for the rigid model in regular waves with prescribed wave to height ratio $1/30$ and current $1\,\mathrm{m/s}$.

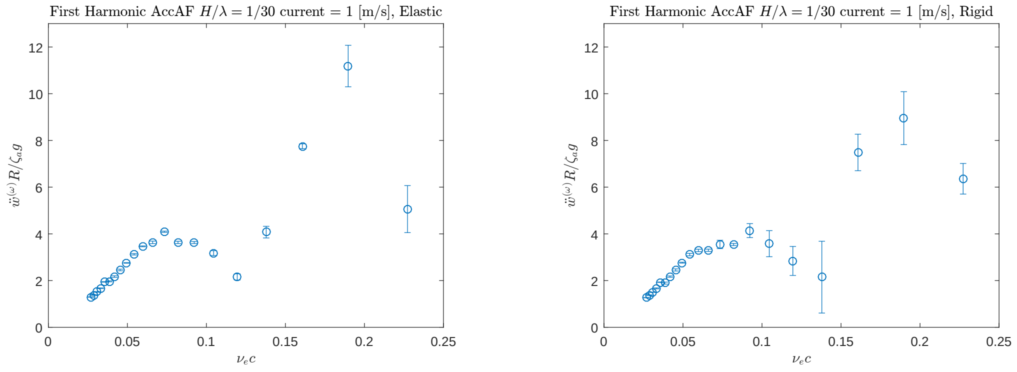

(a) Elastic model (b) Rigid model

Figure 5.31: First harmonic acceleration of the rigid and elastic model in regular waves with prescribed wave to height ratio 1/30, and current 1 m/s. For the accelerometer in the aft position. The non-dimensional wave number are taken from the encounter frequency. The height of the experimental error bars is two times the estimated standard deviation.

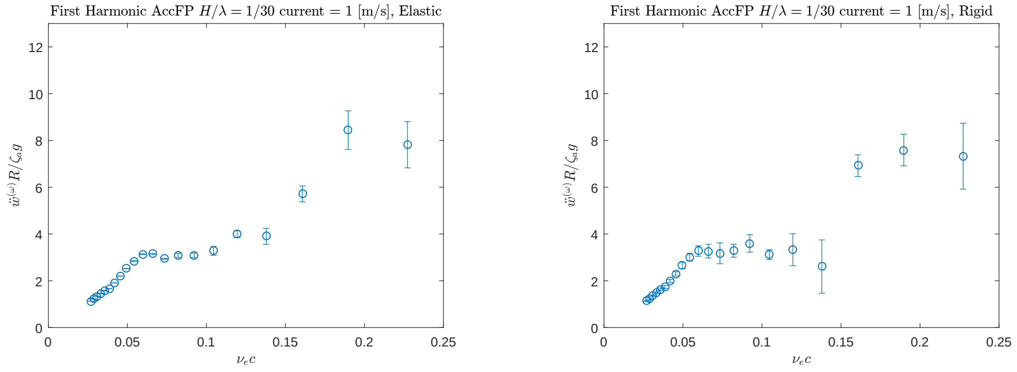

(a) Elastic model (b) Rigid model

Figure 5.32: First harmonic acceleration of the rigid and elastic in regular waves with prescribed wave to height ratio 1/30, and current 1 m/s. For the accelerometer in the front position. The non-dimensional wave number are taken from the encounter frequency. The height of the experimental error bars is two times the estimated standard deviation.

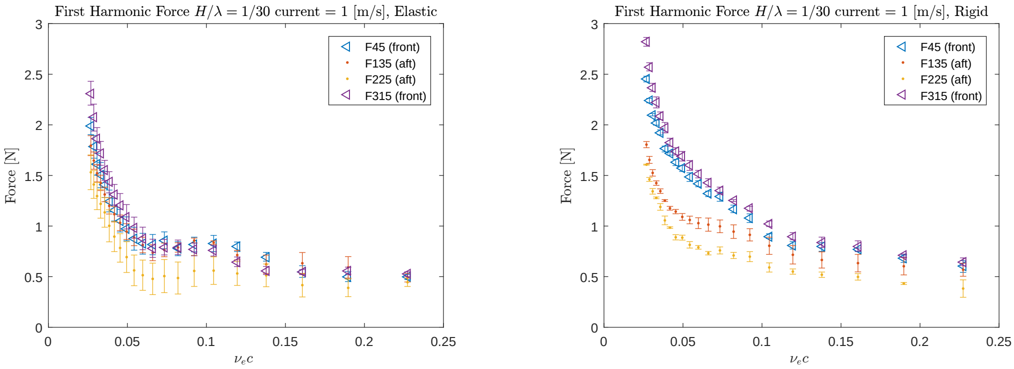

(a) Elastic model

(b) Rigid model

Figure 5.33: Force in the mooring lines for the rigid and elastic model in waves with prescribed wave to height ratio 1/30, and current 1 m/s. The non-dimensional wave number are taken from the encounter frequency. The height of the experimental error bars is two times the estimated standard deviation.

Comparison of the vertical acceleration in Figure 5.31 and 5.32 shows that the vertical acceleration for the rigid and elastic model is similar. The amplitude of the vertical accelerations are found to be larger when current is present compared with the experimental result for the regular wave test.

In Figure 5.33 it is seen that the current will lead to a higher mooring force compared with regular waves only, for both models. This is expected since the current will lead to a mean vertical force on the island. The amplitude of the mooring force is similar for the rigid and elastic model. The trend however is different. For the elastic model the amplitude of the force has a similar shape compared with the experimental results in regular waves. The trend for the rigid model shows that there is a clear different in the mooring front and aft.

5.8 Discussion of the Regular Results

Comparison of the results for the vertical acceleration for the rigid model with and without pressure shows that the pressure has an influence on the result. The regular wave test for the elastic model were repeated eight times over several days.

Therefore, there may have been variation in the pressure out from the compressor, which leads to uncertainties in the result. The other regular test was performed at the same day and is therefore expected to have a smaller variation in the pressure out from the compressor.

In the experiment, the pressure under the air cushion had an influence on the static behavior of the model. The pressure lifts the model and expose the skirt. Therefore, the model is no longer symmetrical in the water line and can lead to unsymmetrical behavior for the vertical acceleration which is seen for the elastic model. The experimental pressure correspond to a full scale pressure between $0.5\,\mathrm{bar} - 1.5\,\mathrm{bar}$. The pressure is much higher than the pressure proposed in the design. Therefore, the effect of the overpressure may not be so critical for the full scale solar island.

To verify the analyzing process of the experimental result, the elastic torus is compared with the result from (Li, 2017). The results for the vertical acceleration and motion are found to be inn good agreement. Comparison of the experimental results from the regular wave test shows that the membrane has an influence on the dynamical behavior. The membrane will increase the amplitude of the first harmonic acceleration and mooring force. The increase in the values needs to be considered in the design process of the island.

The vertical response is found to be lower for high wave frequency when the membrane is presence and higher for low wave frequency, this is the same result as found in Pinkster and Fauzi (1997). The result can be used in the determination of possible location where you want to find sea states that are in the region with low response.

The experimental result shows that the pitch motion of the elastic and rigid model is similar, while the numerical model shows that there is a different. In the numerical model the contribution in bending stiffness due to membrane is not considered. The increase in bending stiffness would lead to lower values of the pitch response. The contribution in stiffness can also be greater for the elastic model, and explain why the experimental result is so similar. The numerical model used to compare the experimental result is to simple too drawn any conclusions.

Another explanation for the similar result between the rigid and elastic model can be due to the pressure. From the experimental result of the vertical acceleration for the elastic model it is shown that the accelerations are no longer symmetrical around the tours. This will also affect the pitch result since the accelerations is used in the calculations.

The largest different for the elastic and rigid model is in the global behavior. The rigid model is not able to undulate with the waves and is therefore more exposed to jerks and slamming. This should be taken into consideration when further develop the design as it can lead to fatigue.

The influence of the skirt in current is not known based on these two experiments and needs to be investigated further to explain the difference in the result between regular waves with current and without current. The interaction between current and skirt may lead to flow separation and viscous effects becomes important. Figure 5.34 shows a sketch of the possible behavior if the skirt in current and waves.

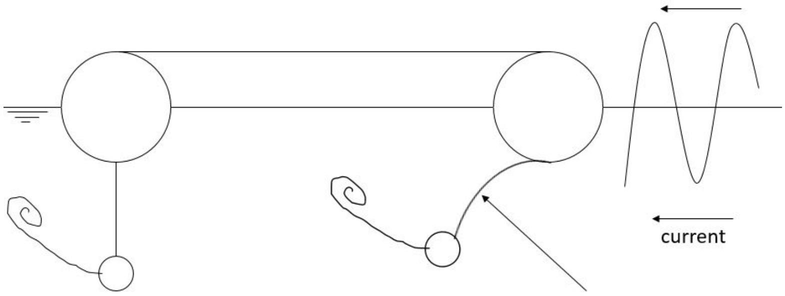

Figure 5.34: A sketch of the thought behavior of the skirt in waves and current.

5.9 Irregular Wave Test

The experimental results for the irregular wave test will be presented as a power spectral density of the measured time history signal.

5.9.1 Constant T_p and Varying H_s

Figure 5.35 shows the acceleration spectrum for the acceleration aft for the elastic and rigid model. Figure 5.36 shows the force spectrum for the forces in mooring line F45 for the elastic and rigid model. Figure 5.37 shows the power spectral density for wave probe 5 compared with the theoretical JONSWAP input spectrum for $H_s = 5\,\mathrm{m}$ and $T_p = 12\,\mathrm{s}$. Figure 5.38 shows the acceleration spectrum for the eight accelerometers used in the experiment for wave condition $H_s = 5\,\mathrm{m}$ and $T_p = 12\,\mathrm{s}$. The power spectral density to all the measurement for the elastic model is given in appendix D.

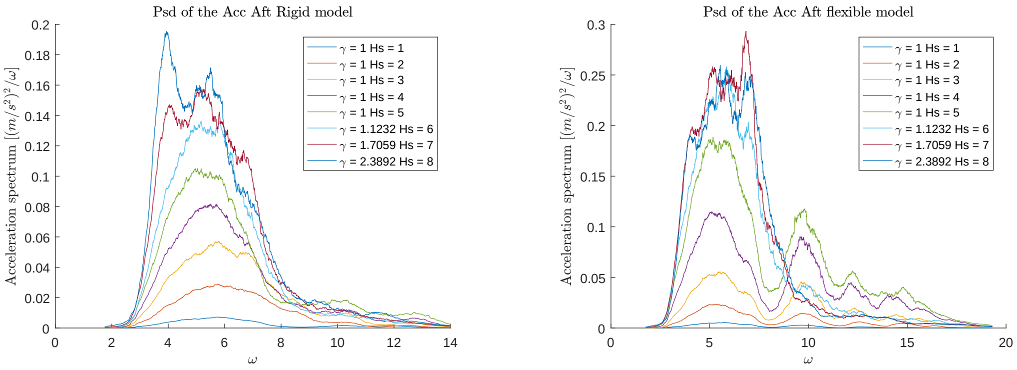

(a) Rigid model (b) Elastic model

Figure 5.35: Power spectral density for the acceleration in the irregular sea states. Both the models were flooded when $H_s > 5\,\mathrm{m}$.

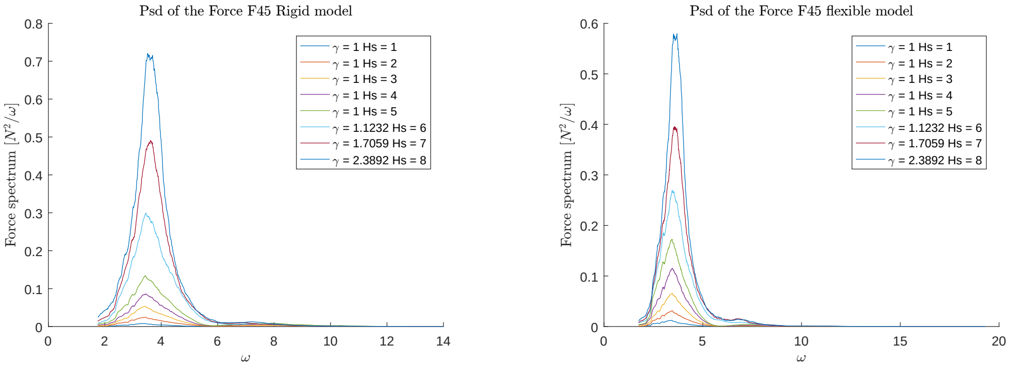

(a) Rigid model (b) Elastic model

Figure 5.36: Power spectral density for the mooring force F45 in the irregular sea states.

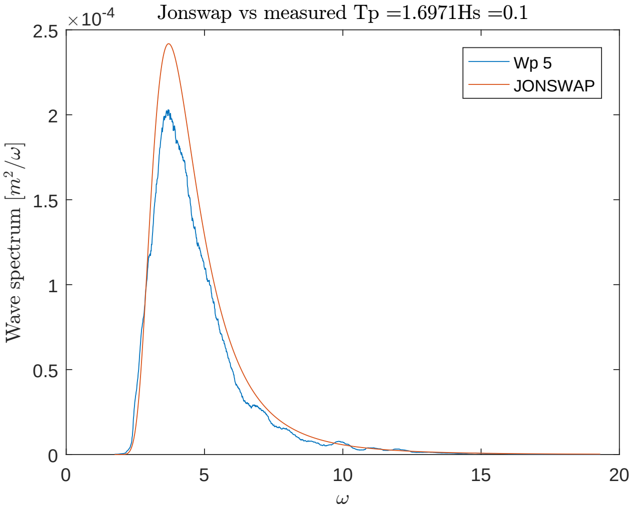

Figure 5.37: Power spectral density for wave probe 5 compared to the input JONSWAP spectrum for $H_s = 5\,\text{m}$ and $T_p = 12\,\text{s}$ in full scale, elastic model.

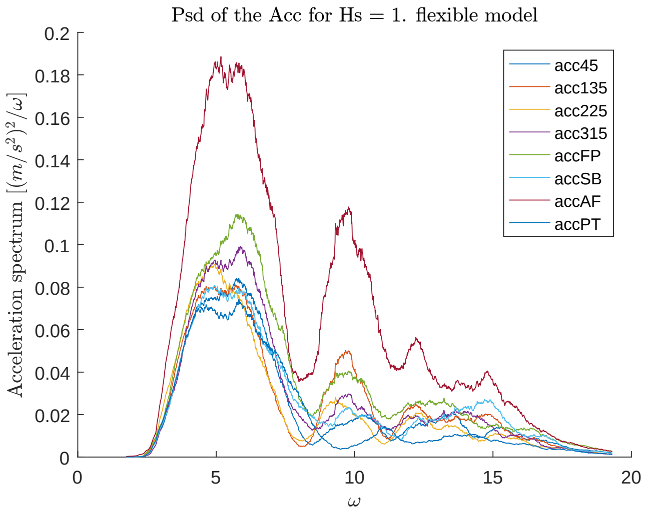

Figure 5.38: Power spectral density for the eight accelerometers in irregular sea states condition $H_s = 5\,\mathrm{m}$ and $T_p = 12\,\mathrm{s}$, elastic model.

5.9.2 Results from the West Africa Region

Figure 5.39 shows the power spectral density of the wave probe 5 for the different region in West Africa compared with the input JONSWAP spectrum. Figure 5.40 shows the power spectral density for the elastic model acceleration fore. Figure 5.41 shows the power spectral density for the heave motion for the elastic and rigid model in Angola(swell) conditions. Figure 5.42 shows the response amplitude operator in heave calculated by Equation (4.6).

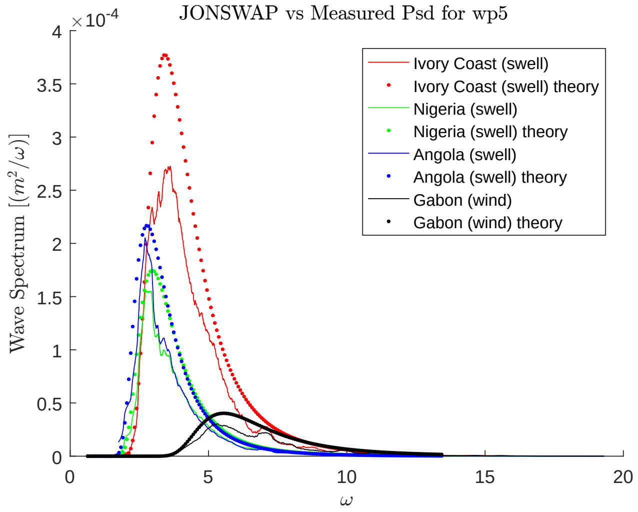

Figure 5.39: Power spectral density for wave probe 5 compared with the JONSWAP spectrum for Ivory Coast, Nigeria, Angola and Gabon.

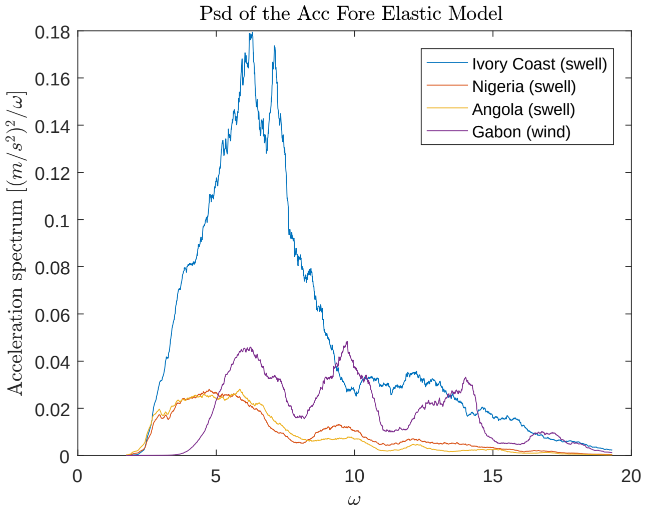

Figure 5.40: Power spectral density for the acceleration fore for the elastic model, in wave condition for Ivory Coast, Nigeria, Angola and Gabon.

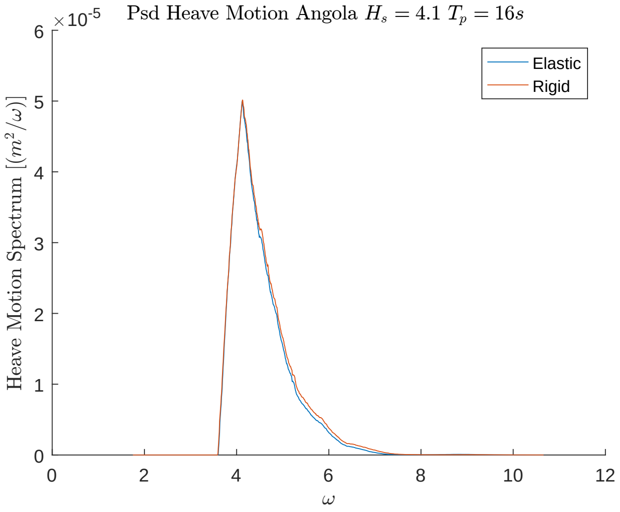

Figure 5.41: Power spectral density for the heave motion for the elastic and rigid model, in Angola (swell) wave condition.

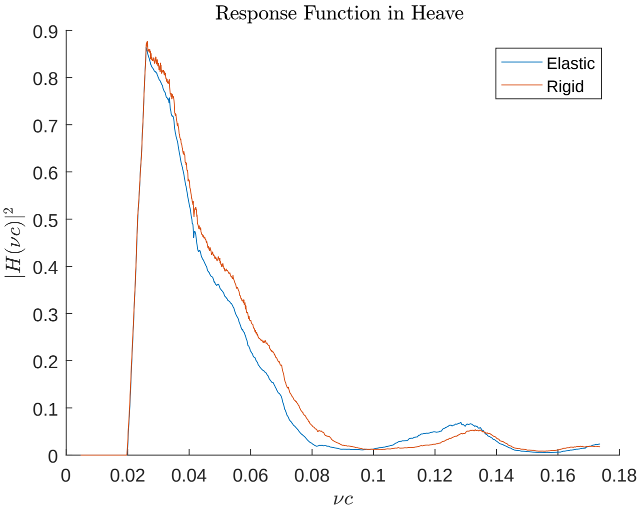

Figure 5.42: Response amplitude operator for heave calculated from the irregular wave test by use of Equation (4.6) for the rigid an elastic model. The input and measured response function are from Angola.

5.9.3 Discussion of the Irregular Results

Both the models was completely flooded when the significant wave height was larger than, $H_s > 5\,\mathrm{m}$, and peak period, $T_p = 12\,\mathrm{s}$. Failure also occurred for the elastic and rigid model in wave conditions for Ivory Coast. The power spectral density in Figure 5.36 shows that the acceleration on the elastic model is little higher. This can indicate that the pressure was higher for the elastic model during the irregular wave test. In the elastic model the acceleration has a second peak for wave frequencies $\omega = 10\,\mathrm{rad/s}$. This can be due to the peak that is shown in the response amplitude operator for the heave motion at $\omega = 10\,\mathrm{rad/s}$. Figure 5.38 shows that all eight accelerometers has the same peak, but the value is larger for the acceleration aft. The peak vanishes after flooding of the structure has occurred.

The comparison between the measured wave spectrum and the JONSWAP spectrum shown in Figure 5.39 and 5.37, shows that the experimental peak are less than the input spectrum. This can be caused by wave breaking and viscous effects that can be developed across the tank. The difference for Ivory Coast is probably not due to wave breaking since H/λ is far from the breaking limit. The results should therefore be investigated further.

The response amplitude operator in heave, Figure 5.42, which is calculated from Equation (4.6) are in reasonable agreement with the RAO in heave found from the regular wave test.

5.10 Error Sources

The largest uncertainty during the experiment is the pressure inside the air cushion. The value of the output pressure would be unphysical inside the air cushion. In addition the output pressure was read manually by eye and the accuracy of the reading is $\pm 0.01\,\mathrm{bar}$, so the pressure during the different wave test can be different for each run. As seen in the result the pressure has an influence on the experimental result.

A check of the wave generation without the model were not preformed, and this leads to uncertainty in the analyses of the result. Since the wave amplitude from the experiment are used in the analysis of the result. Therefore, a calibration of the waves, before the model test should have been performed. Small steep waves tend to be unstable and can change radically with the distance from the wave maker, due to wave breaking and viscous effects. A consequence can be that there are significant deviations in wave amplitude across the tank (Steen, 2014). Other possible reasons for the difference in the wave measurements are wave reflection from the beach, meniscus effect on the wave probe wire and calibration linearity error.

The instruments can drift due to temperature, splashes etc. This will lead to that the measurement will have a non-zero value. This is especially important for the mooring force in waves and current. The drifting problem is normal for the acceleration used in this experiment. The accelerometers used is body-fixed and can only measure the acceleration in one direction. The round surface of the floater made it hard to attached the accelerometers perfect and a slight angle between the horizontal axes will effect the result.

The mooring of the elastic tours can cause the torus to be deformed, and this will affect the result. Another error source is that the pre-tension in the mooring lines were too low. Too low pre-tension will lead to slack in the line and the weight of the spring is measured and not the actual force. This was observed for the irregular wave test for $H_s = 6\,\mathrm{m}$ and $T_p = 12\,\mathrm{s}$.

The waiting time between each wave test were at least 3 min in order to damp out the waves. The damping beach showed to be effective for damping out waves and making the water surface calm after each test run. Still standing waves can have occurred and influencing the result.

Chapter 6

Conclusions

The dynamical behavior of a floating solar island is studied through model tested in current, and both regular and irregular waves. Two different configurations of the solar island were investigated; a model made with an elastic torus and a model with a rigid torus. During the experiment, vertical acceleration was measured, forces in the mooring lines and the wave elevation. A camera is used to capture the global behavior of the model. To support the experimental result a numerical model for the vertical response is made by combining theory for a floating torus and the vertical motion of a Surface Effect Ship (SES).

The global behavior of the rigid and elastic model in waves is investigated and found different. The elastic model is more capable of following the waves. For both models, non-linear phenomena such as out of water and over-topping of waves were observed. Both models were flooded in regular waves with period 12.1 s and steepness = 1/20, and in irregular waves with $T_p = 12\,\mathrm{s}$ and $H_s > 5\,\mathrm{m}$.

There is good agreement between the experimental result and the numerical model for the heave response. The results show that the membrane covering the torus will lead to a higher vertical response for low wave frequencies, and reduction for high wave frequency. The use of elastic and rigid torus has little influence on the vertical response for the solar island.

The experimental results for the vertical acceleration is largest at front and aft. The results show that the membrane and pressure is increasing the vertical acceleration. The largest vertical accelerations are found for the rigid model with pressure and the elastic model. Second harmonic accelerations were found to matter for the elastic and rigid model.

The force in the mooring lines is also affected by the air cushion. The air cushion is increasing the force in the mooring lines. The skirt that used to prevent the air leakage is also reducing the horizontal motion due to the increasing in added mass in surge.

A check of the wave generation without the present of the model should have been executed. The result from the wave probes shows that the measured wave spectrum has a lower peak than the input spectrum. From the regular test the model is found to have little wave generation. The biggest error sources in the experiment is the unknown pressure under the air cushion. The applied pressure causes a static instability for both models. Due to pressure, the islands are no longer symmetrical in the water line.

Chapter 7

Recommendation for Further Work

- Further development of the numerical model to include the effect of membrane and skirt in vertical and horizontal direction. Also include coupling between the horizontal and vertical motion.
- Repetition of the experiment with a pressure measurement underneath the membrane.
- Investigation of the skirt behavior in waves and current.
- Investigation of the experimental results from the irregular wave test.
- Development of the design to increase the survivability for the island in waves, and a more thorough investigation for all the possible areas for the solar island.
- Investigate other possibilities to support the weight of the PV panels, without use of pressure.

Bibliography

Abramowitz, M. & Stegun, I. A. (1964). *Handbook of mathematical functions: with formulas, graphs, and mathematical tables.* Courier Corporation.

Choi, Y.-K. (2014). A study on power generation analysis of floating pv system considering environmental impact. *development*, *8*(1).

CSEM. (2007). Scientific and technical report 2007.

Dean, R. G. & Dalrymple, R. A. (1991). *Water wave mechanics for engineers and scientists.* World Scientific Publishing Co Inc.

DNV. (2013). Dnv-os-e301 position mooring. DNV.

DNV. (2014). Edv-rp-c205 enviromental conditions and environmental loads. DNV.

Dong, G.-h., Hao, S.-h., Zhao, Y.-p., Zong, Z., & Gui, F.-k. (2010). Elastic responses of a flotation ring in water waves. *Journal of Fluids and Structures*, *26*(1), 176–192. doi:http://dx.doi.org/10.1016/j.jfluidstructs.2009.09.001

Faltinsen, O. (1993). *Sea loads on ships and offshore structures.* Cambridge university press.

Faltinsen, O. M. [Odd M]. (2005). *Hydrodynamics of high-speed marine vehicles.* Cambridge university press.

Faltinsen, O. M. [Odd M.]. (2011). Hydrodynamic aspects of a floating fish farm with circular collar. *The 26th International Workshop on Water Waves and Floating Bodies (IWWFB). April 17-20. Athens, Greece.*

Faltinsen, O. M. [Odd M.]. (2012, March 9). Added mass, damping and wave excitation loads on a semi-submerged elastic torus (tori) at small frequencies.

Greco, M. (2016, July 26). *Tmr4215: sea loads lecture notes.*

Hogben, N., Olliver, G. F., Dacunha, N. M. C., & British Maritime Technology, L. (1986). *Global wave statistics.* Old Working: Published for British Maritime Technology by Unwin Brothers Limited.

Hughes, S. A. (1993). *Physical models and laboratory techniques in coastal engineering.* World Scientific.

Larsen, C. M. & Norges teknisk-naturvitenskapelige universitet Institutt for marin, t. (2012). *Marin dynamikk : kompendium for bruk i faget tmr 4182 marin dynamikk ved institutt for marin teknikk, fakultet for ingeniørvitenskap og teknologi, ntnu.* TMR4182 Marin dynamikk. Trondheim: Marinteknisk senter, Institutt for marin teknikk.

Lee, C.-H. & Newman, J. (2000). Wave effects on large floating structures with air cushions. *Marine Structures*, *13*(4–5), 315–330. Very Large Floating Structures (VLFS) Part I. doi:https://doi.org/10.1016/S0951-8339(00)00014-9

Li, P. (2017). A theoretical and experimental study of wave-induced hydroelastic response of a circular floating collar.

Li, P. & Faltinsen, O. M. [Odd M.]. (2012). Wave-induced vertical response of an elastic circular collar of a floating fish farm. *10th International Conference on Hydrodynamics October 1-4, 2012 St. Petersburg, Russia.*

Li, P., Faltinsen, O. M., & Greco, M. (2014). Wave-induced accelerations of a fish-farm elastic floater: experimental and numerical studies. In *Asme 2014 33rd international conference on ocean, offshore and arctic engineering* (V007T05A004–V007T05A004). American Society of Mechanical Engineers.

Li, P., Faltinsen, O. M., & Lugni, C. (2016). Nonlinear vertical accelerations of a floating torus in regular waves. *Journal of Fluids and Structures*, *66*, 589–608. doi:http://dx.doi.org/10.1016/j.jfluidstructs.2016.08.007

Newman, J. N. (1977a). *Marine hydrodynamics.* MIT press.

Newman, J. N. (1977b). The motions of a floating slender torus. *Journal of Fluid Mechanics*, *83*(04), 721–735.

Pinkster, J. & Fauzi, A. (1997). The effect of air cushions under floating offshore structures. In *Proceedings of the eighth international conference on the behavior of offshore structure* (pp. 143–158).

Pinkster, J. & Scholte, E. M. (2001). The behaviour of a large air-supported mob at sea. *Marine Structures*, *14*(1), 163–179.

Steen, S. (2014). *Experimental methods in marine hydrodynamics.*

Trapani, K. & Redón Santafé, M. (2015). A review of floating photovoltaic installations: 2007–2013. *Progress in Photovoltaics: Research and Applications*, *23*(4), 524–532.

Appendix A

Results for the Elastic Torus with Membrane

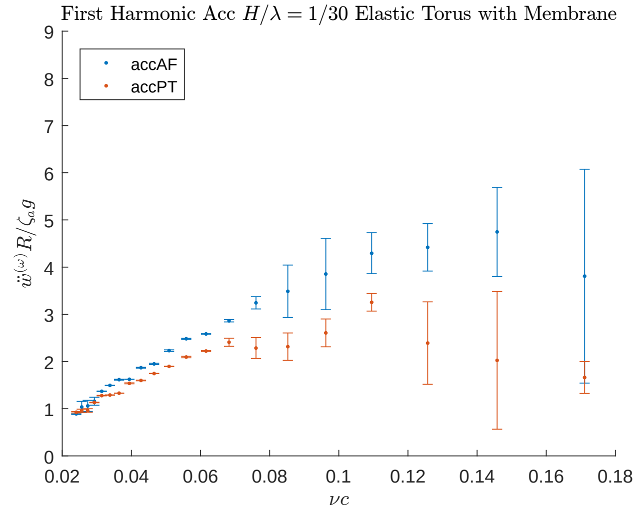

Figure A.1: The elastic torus covered with membrane non-dimensional amplitude of first harmonic vertical acceleration versus the non-dimensional wave number νc for regular waves with steepness $1/30$. At the position front and aft at the model. The height of the experimental error bars is two times the estimated standard deviation.

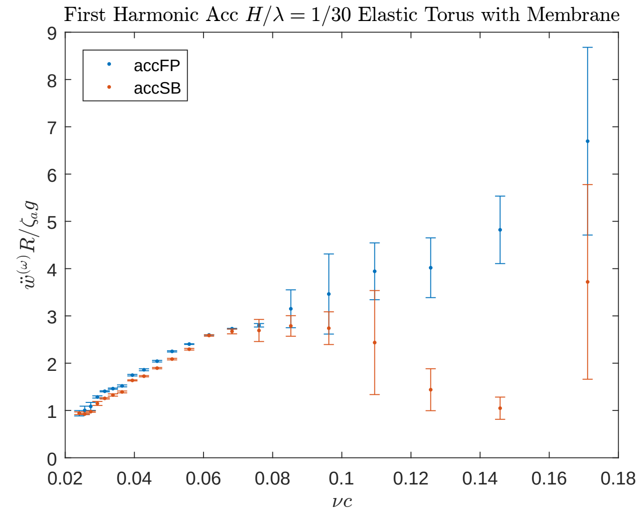

Figure A.2: The elastic torus covered with membrane non-dimensional amplitude of first harmonic vertical acceleration versus the non-dimensional wave number νc for regular waves with steepness $1/30$. At the position left and right side at the model. The height of the experimental error bars is two times the estimated standard deviation.

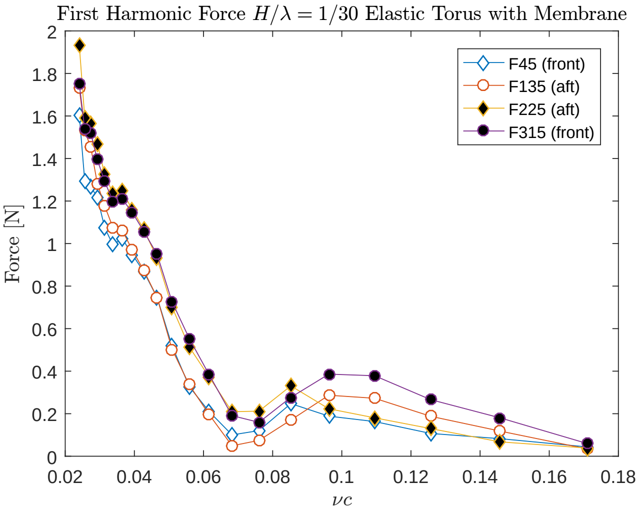

Figure A.3: Amplitude of the force in the four mooring lines for the rigid model without pressure for regular wave steepness $1/30$, elastic torus covered with membrane. The height of the experimental error bars is two times the estimated standard deviation.

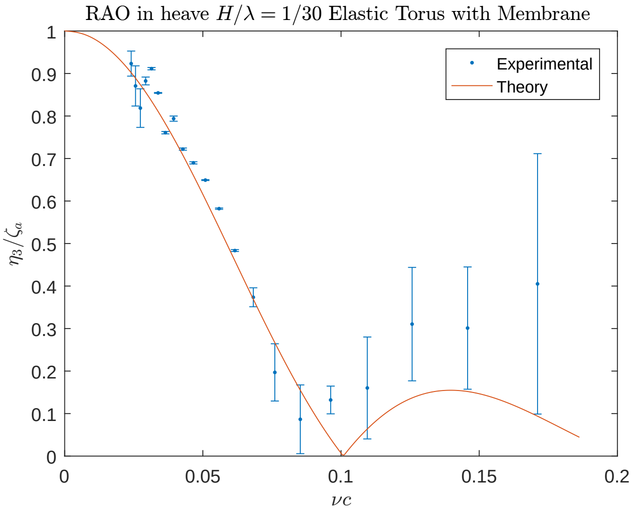

Figure A.4: RAO in heave for the experimental results for the elastic torus covered with membrane for regular waves with steepness 1/30.. The result is compared with the theory for the floating solar island vertical response. The height of the experimental error bars is two times the estimated standard deviation.

Appendix B

Raw Data from the Experiment

B.1 Regular Waves for Elastic Model

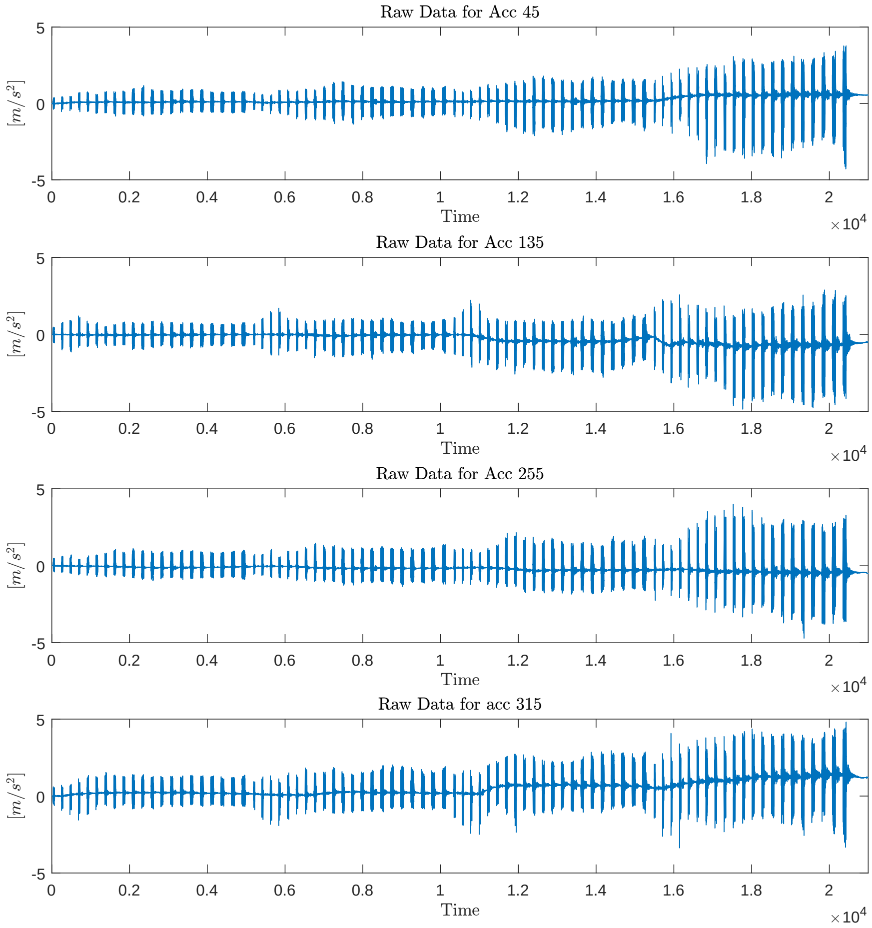

Figure B.1: Raw data of the accelerometers 45, 135, 225 and 315.

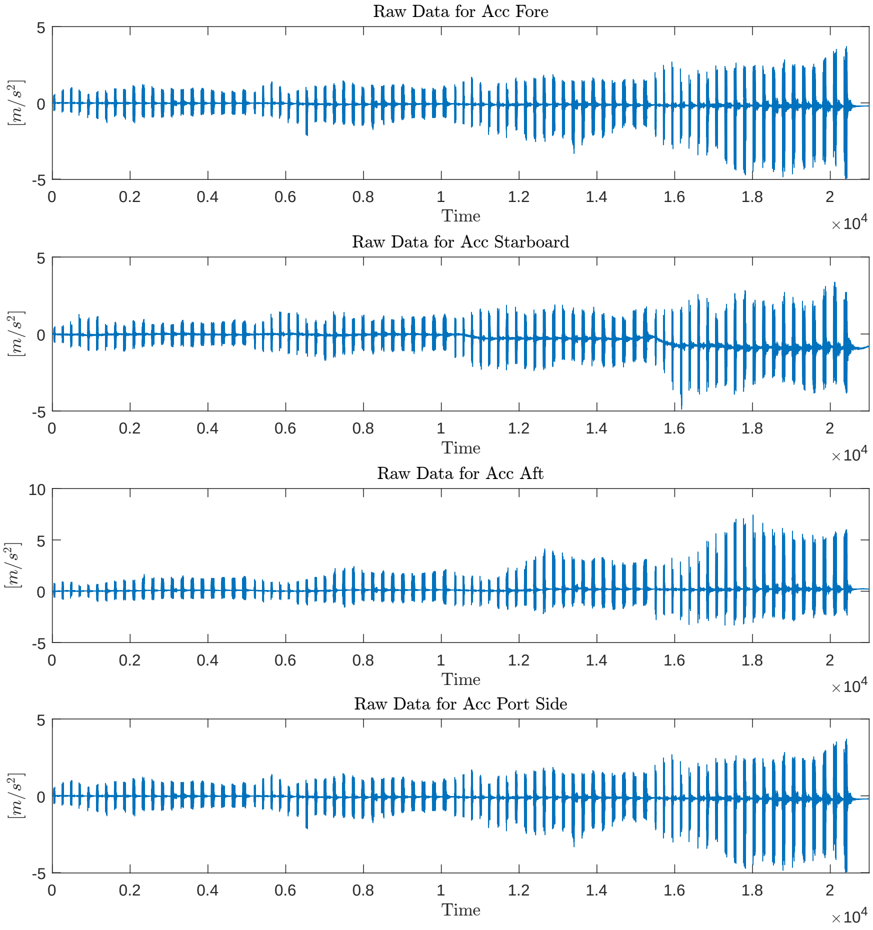

Figure B.2: Raw data of the accelerometers fore, starboard, aft and port side.

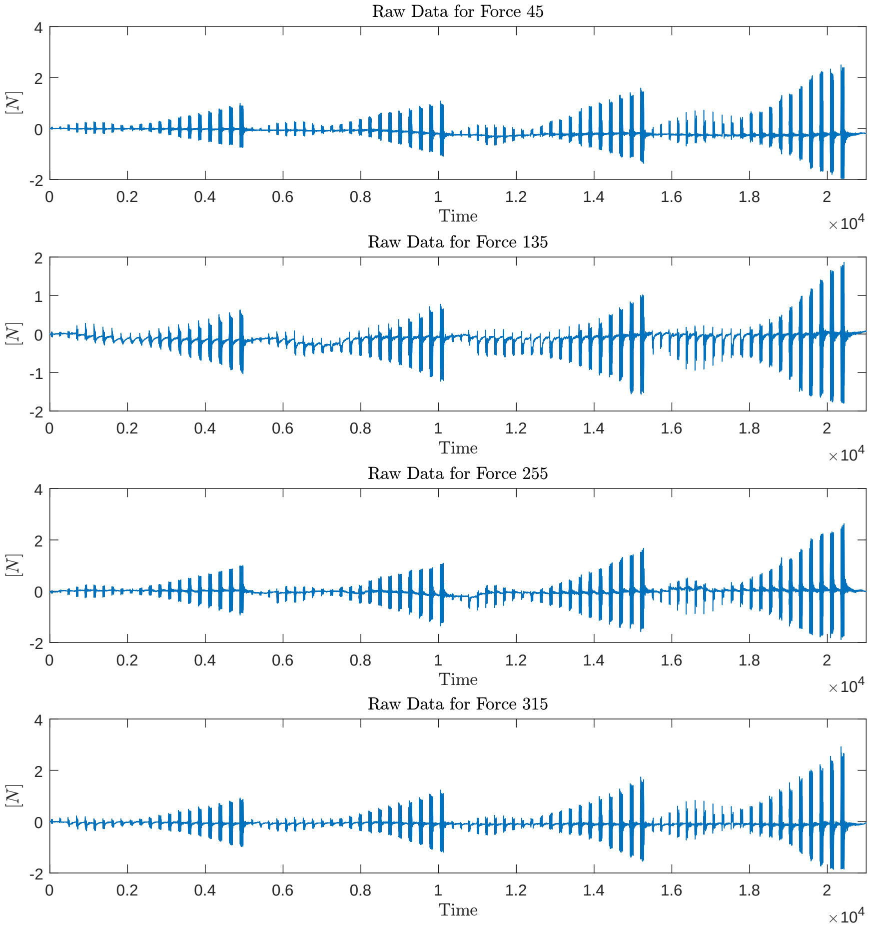

Figure B.3: Raw data of the force.

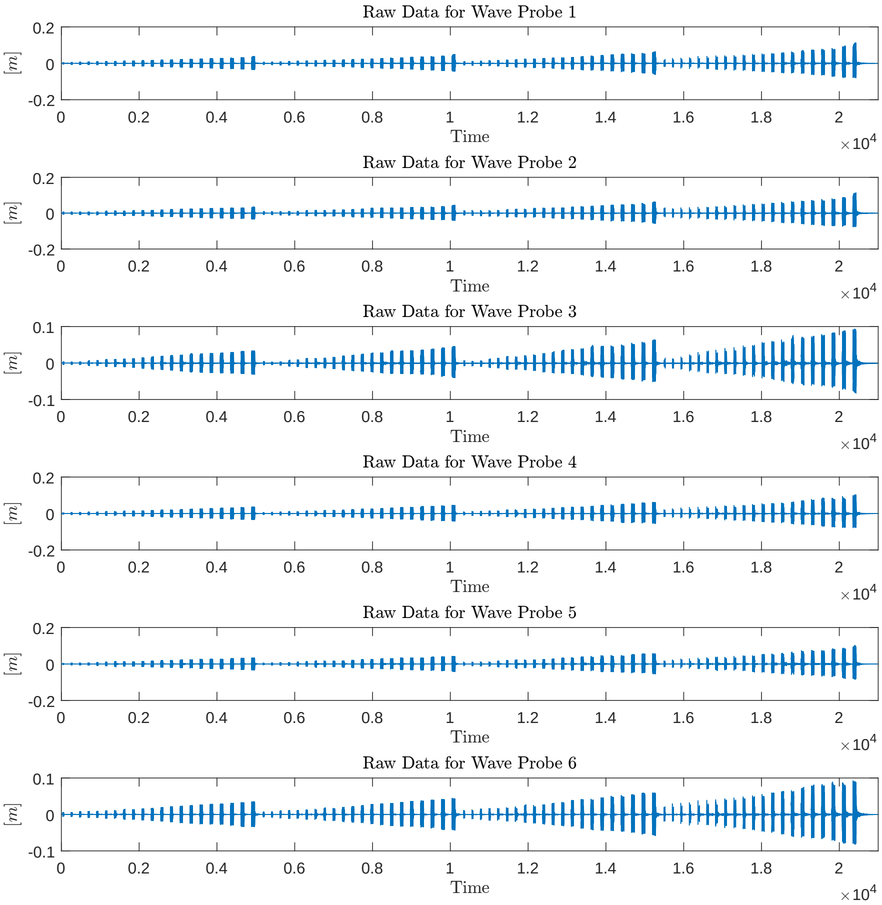

Figure B.4: Raw data of the wave probes.

B.2 Irregular Waves Constant T_p and Varying H_s

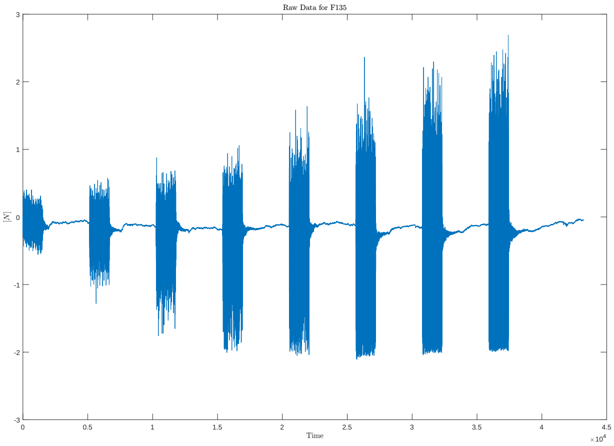

Figure B.5: Raw data for the irregular waves for wave probe 4.

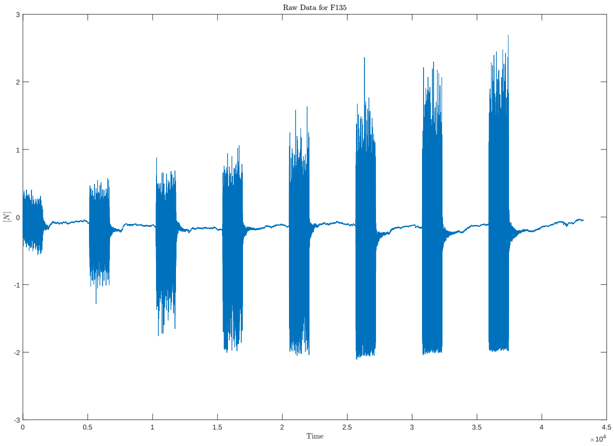

Figure B.6: Raw data for the irregular waves for wave probe 4.

Appendix C

Filtering of data

Figure C.1 and C.2 shows the band-pass filtering of the first and second harmonic. The filter (green line) is multiplied with the data (blue line) to only get the data of interested (red line).

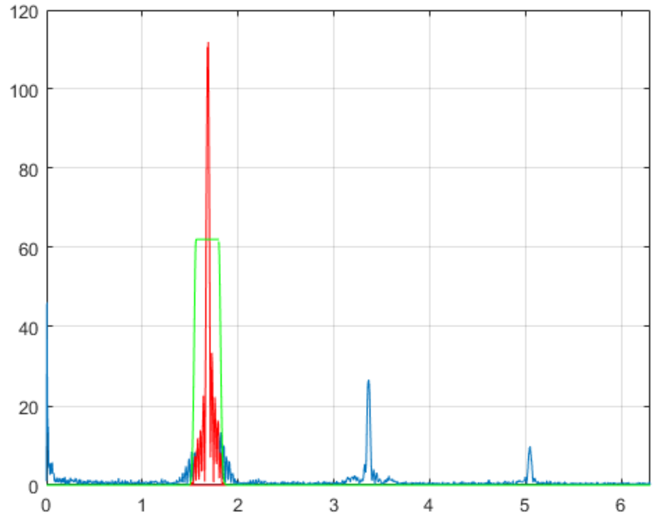

Figure C.1: Example of a band pass filter, filtering out the first harmonic.

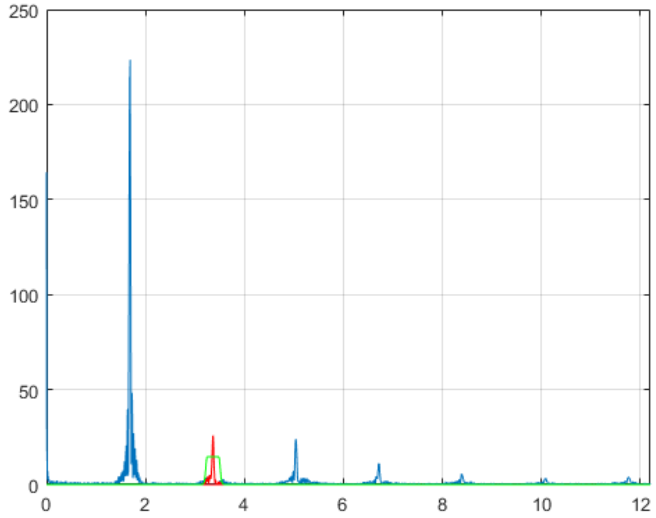

Figure C.2: Example of a filter, filtering out the second harmonic.

Appendix D

Psd for the Irregular Wave Test Elastic Model

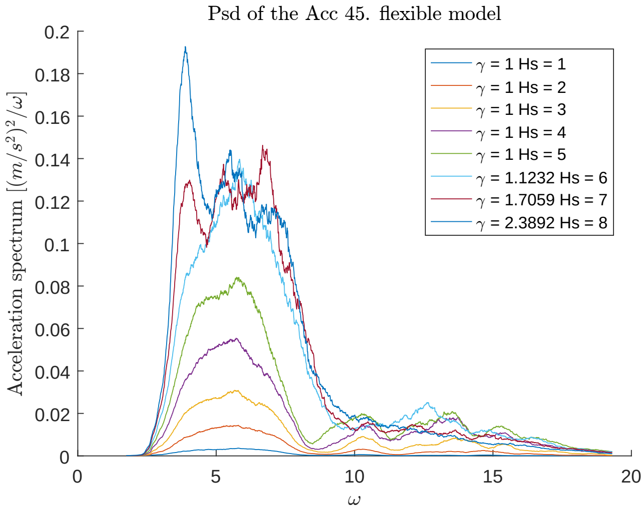

Figure D.1: Power spectral density for the acceleration in irregular sea states, elastic model.

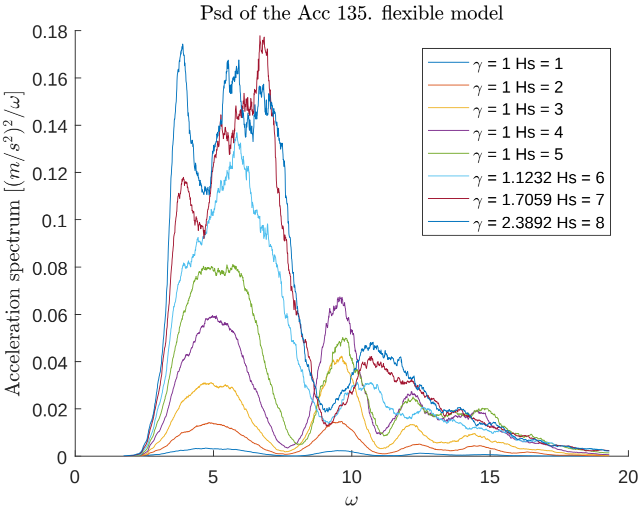

Figure D.2: Power spectral density for the acceleration in irregular sea states, elastic model.

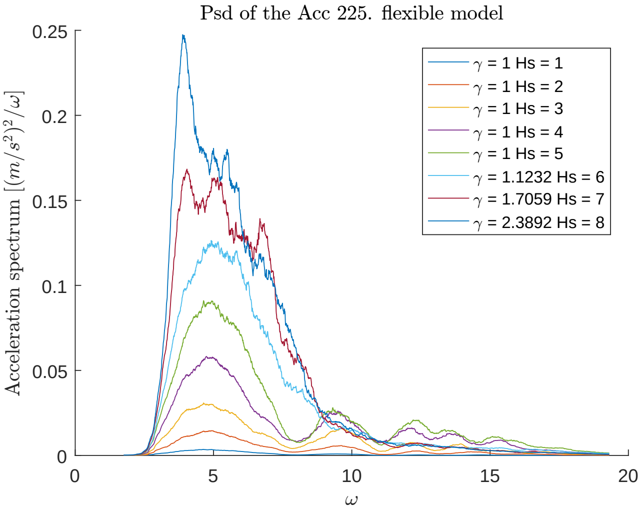

Figure D.3: Power spectral density for the acceleration in irregular sea states, elastic model.

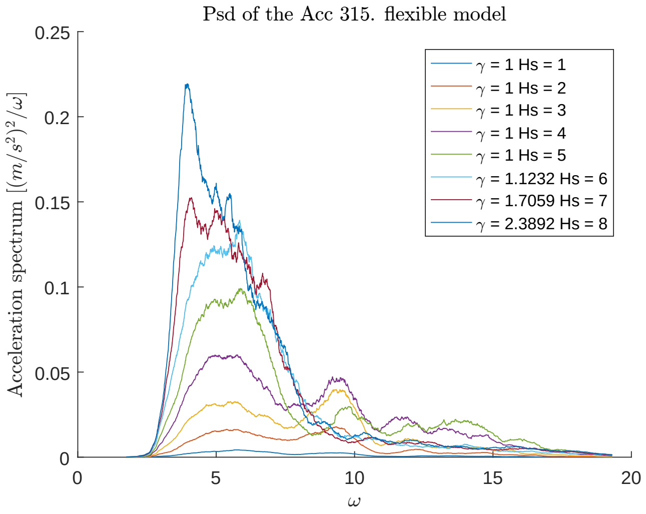

Figure D.4: Power spectral density for the acceleration in irregular sea states, elastic model.

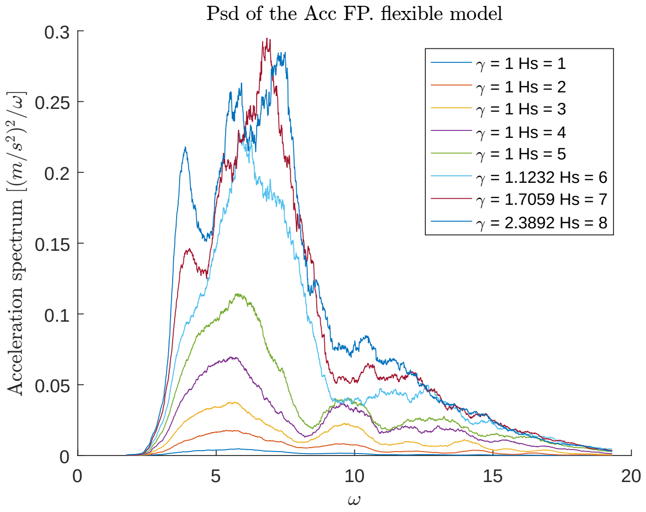

Figure D.5: Power spectral density for the acceleration in irregular sea states, elastic model.

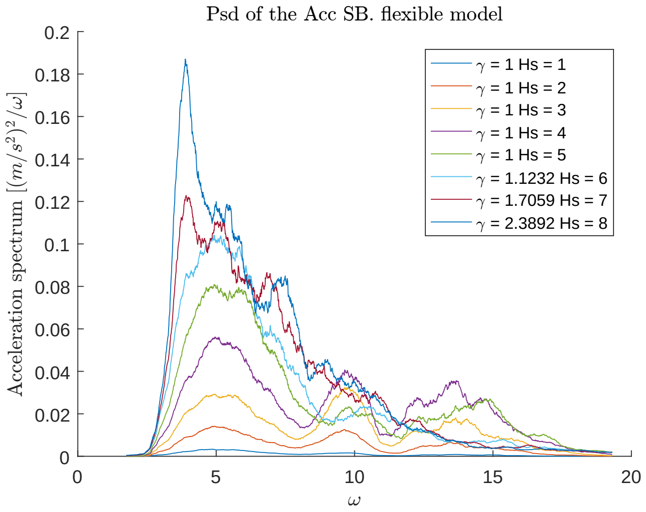

Figure D.6: Power spectral density for the acceleration in irregular sea states, elastic model.

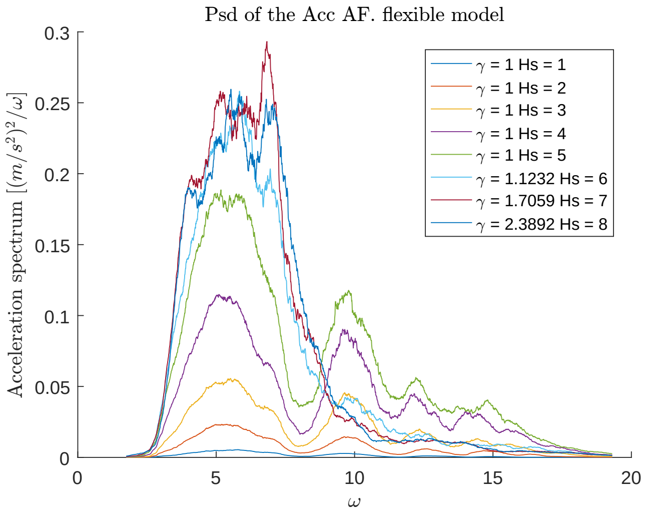

Figure D.7: Power spectral density for the acceleration in irregular sea states, elastic model.

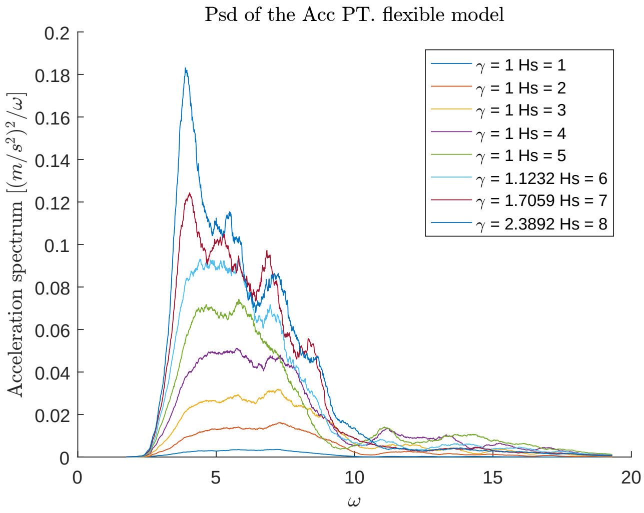

Figure D.8: Power spectral density for the acceleration in irregular sea states, elastic model.

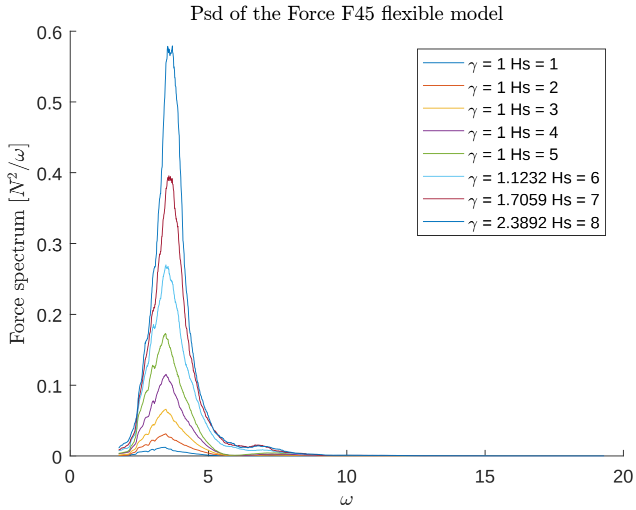

Figure D.9: Power spectral density for the force in irregular sea states, elastic model.

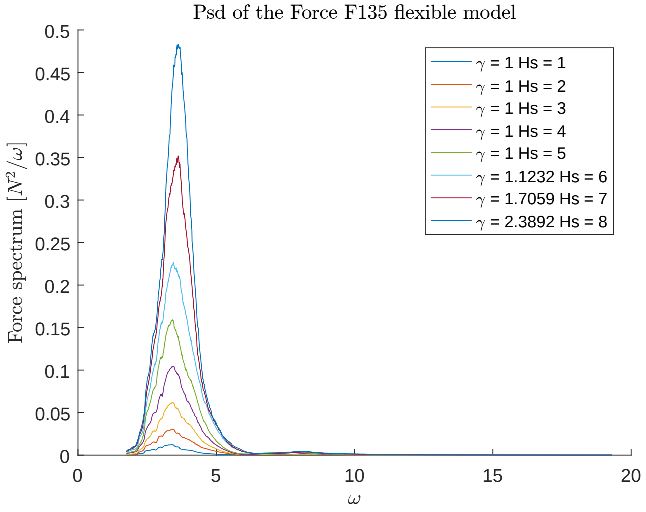

Figure D.10: Power spectral density for the force in irregular sea states, elastic model.

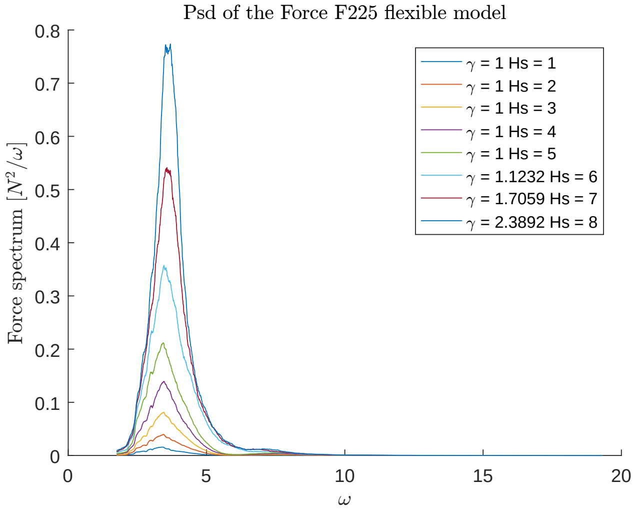

Figure D.11: Power spectral density for the force in irregular sea states, elastic model.

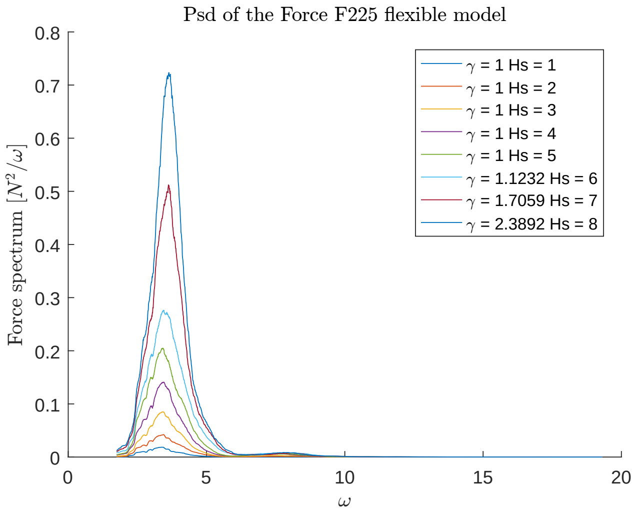

Figure D.12: Power spectral density for the force in irregular sea states, elastic model.

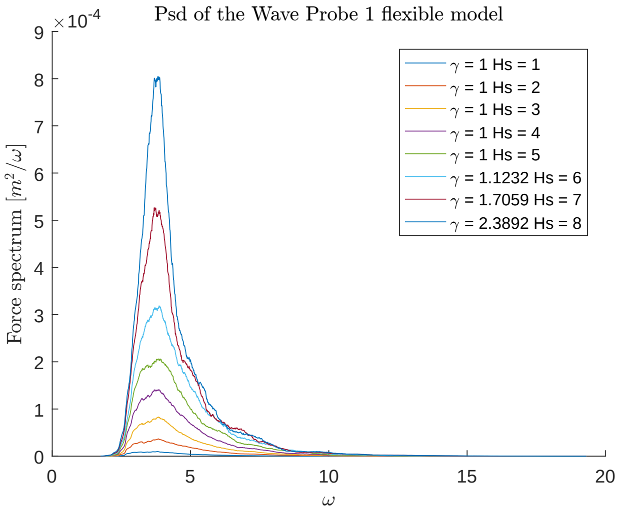

Figure D.13: Power spectral density for the wave probe in irregular sea states, elastic model.

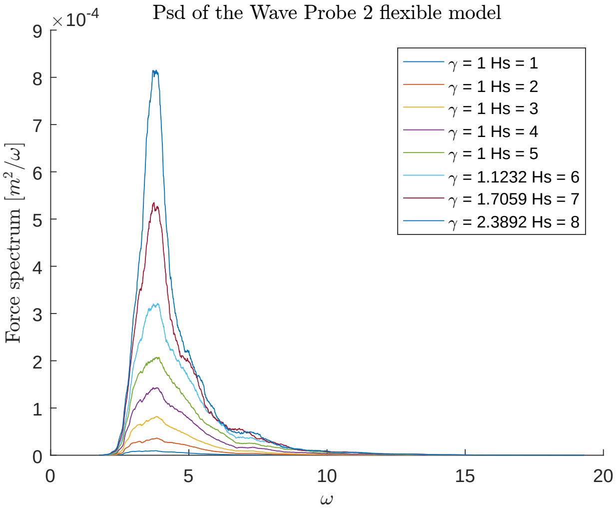

Figure D.14: Power spectral density for the wave probe in irregular sea states, elastic model.

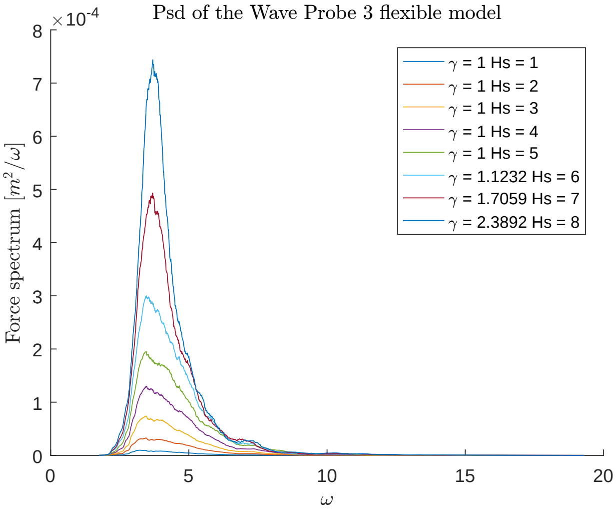

Figure D.15: Power spectral density for the wave probe in irregular sea states, elastic model.

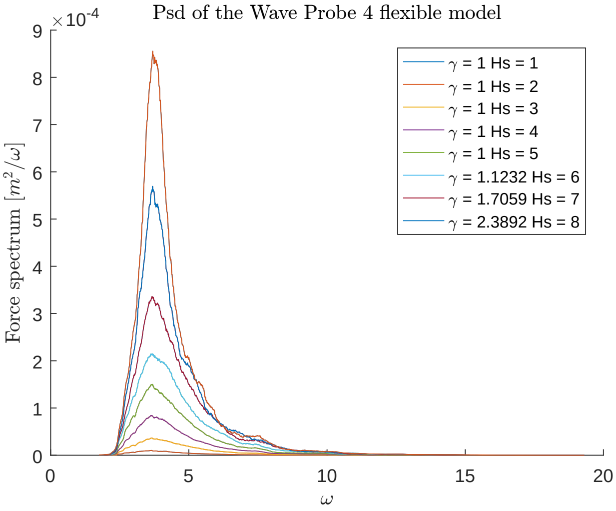

Figure D.16: Power spectral density for the wave probe in irregular sea states, elastic model.

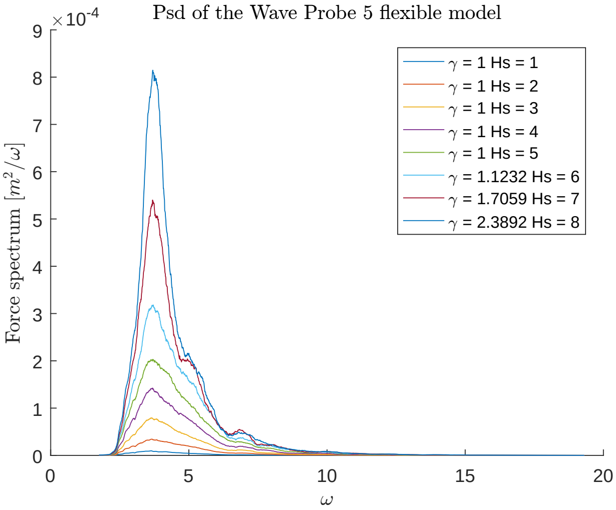

Figure D.17: Power spectral density for the wave probe in irregular sea states, elastic model.

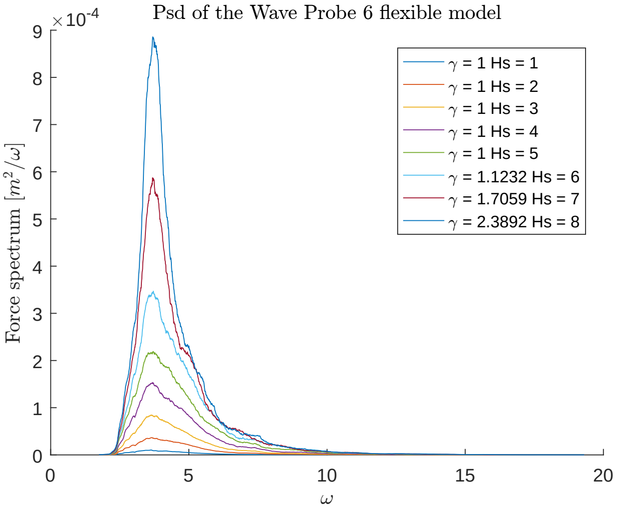

Figure D.18: Power spectral density for the wave probe in irregular sea states, elastic model.